Experimental identification of two distinct skyrmion collapse mechanisms

Florian Muckel,[1,†] Stephan von Malottki,[2,†] Christian Holl,[1] Benjamin Pestka,[1]
Marco Pratzer,[1] Pavel F. Bessarab,[3,4,5] Stefan Heinze,[2] and Markus Morgenstern[1,*]

[1] *II. Institute of Physics B and JARA-FIT, RWTH Aachen University, D-52074 Aachen, Germany*
[2] *Institute of Theoretical Physics and Astrophysics, University of Kiel, Leibnizstrasse 15, 24098 Kiel, Germany*
[3] *Science Institute of the University of Iceland, 107 Reykjavík, Iceland*
[4] *ITMO University, 197101 St. Petersburg, Russia*
[5] *Peter Grünberg Institute and Institute for Advanced Simulation, Forschungszentrum Jülich, 52425 Jülich, Germany*

Magnetic skyrmions are key candidates for applications in memory, logic, and neuromorphic computing. An essential property is their topological protection caused by the swirling spin texture and described by a robust integer winding number. However, this protection is only strictly enforced in the continuum, and so the atomic lattice present in all real materials leaves a loophole for switching the winding number. Hence, understanding the microscopic mechanism of this unwinding is crucial for enhancing the stability of skyrmions. Here, we use spin polarized scanning tunneling microscopy to locally probe skyrmion annihilation by individual hot electrons. We tune the collapse rate by up to four orders of magnitude using an in-plane magnetic field, and observe distinct transition rate maps that are either radially symmetric or exhibit an excentric hot spot. We compare these maps to first-principles based atomistic spin simulations and find that they are explained by a radially symmetric collapse at zero in-plane field and a transition to the recently predicted chimera collapse at finite in-plane magnetic fields. These insights into the transient state of the skyrmion collapse will enable future enhancement of skyrmion stability and designs for intentional skyrmion switches.

The topological protection of skyrmions [1, 2] implies large stability during manipulation [3, 4]. The additional possibility to provide magnetic skyrmions up to room temperature by stacking ultrathin transition-metal films [5–7] as well as to control skyrmion creation and subsequent transport at relatively low current density [6, 8] established them as key candidates for race-track memories or logic devices [3, 4] and prospective for synaptic network electronics [9]. However, the stability of the skyrmions, not rigorously protected by topology [10, 11], is a key challenge [12, 13]. While a small skyrmion size is mandatory for favorable storage density and energy efficiency [3, 4], theory predicts that the energy barrier preventing skyrmion collapse can strongly decrease with reduced skyrmion size [11, 14]. Experimentally, intriguing results have been found regarding the Arrhenius prefactor of the skyrmion collapse rate that varies by 30 orders of magnitude with out-of-plane magnetic field [15] and showcases a strong dependence on local disorder [8, 16, 17]. The central handle to probe the skyrmion dynamics experimentally is real space mapping [2, 5–7, 12, 18–29] employed to reveal controlled writing and deleting [22, 29], creation at defects via spin currents [6, 30], current induced longitudinal and transversal motion [6, 7, 28] as well as excitation modes [26, 27]. Most advanced, spin-polarized scanning tunneling microscopy (SP-STM) [5, 22–25] provided guiding insights for the paradigmatic Pd/Fe bilayer on Ir(111) [22, 23, 31] that exhibits ultra-small, isolated Néel skyrmions [22] often pinned at atomic defects within the Pd layer [22, 32]. Its current-induced collapse has been probed [22, 31] and subsequently compared to Monte Carlo simulations without pinpointing the mechanism [31].

Independent of experiments, atomistic spin simulations based on parameters from density functional theory (DFT) found a strong entropy contribution to the collapse prefactor [33, 34] and key contributions to the energy barrier by exchange frustration [35], higher-order exchange interactions [36] or the presence of defects [37]. In addition, a novel collapse mechanism besides the conventionally assumed radial symmetric collapse has been predicted [25, 38], coined the chimera mode due to the intermediate state with an unconventional dipolar topological charge (Fig. 1f). However, none of these intriguing predictions has been confirmed experimentally.

Here, we demonstrate experimentally that both, the radial symmetric and the chimera-type collapse indeed exist. We map the current induced skyrmion collapse rate of the model system Pd/Fe/Ir(111) with sub-nm resolution by SP-STM [39]. We show that the collapse probability per injected electron exhibits an angularly symmetric map for zero in-plane magnetic field and becomes strongly asymmetric with applied in-plane fields. This is straightforwardly explained by the energy distributions required for the transition state of the radial symmetric and chimera type collapse, as calculated via an advanced atomistic spin model parametrized by DFT results, while using the geodesic nudged elastic band (GNEB) approach

† These authors contributed equally to this work
* mmorgens@physik.rwth-aachen.de

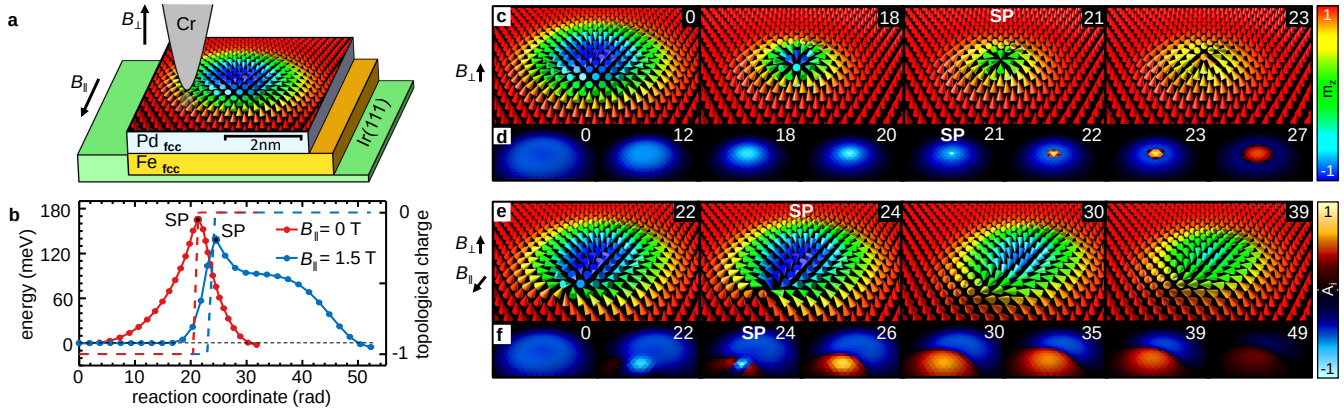

Figure 1. **Radial symmetric and chimera collapse mechanism. a**, Sketch of the STM experiment performed on a stack of Ir(111) covered by one Fe monolayer and one Pd monolayer with displayed magnetization vectors of the skyrmion on top (color code on the right of (c)), B fields, $B_\parallel$ and $B_\perp$, that tune the skyrmion collapse are indicated. **b**, Energy relative to the initial state (dots) and total topological charge $Q_{\text{topo}} = \sum_i A_i$ (dashed lines, methods) evaluated for subsequently numbered images along the minimum energy path as deduced by GNEB for, both, the radial symmetric collapse (red) at $B_\parallel = 0\,\text{T}$ and the chimera type collapse (blue) at $B_\parallel = 1.5\,\text{T}$, both curves: $B_\perp = 3.2\,\text{T}$. Saddle points SP are marked. **c** Selected calculated images from the minimum energy path of (b) displaying the magnetization vectors for the radial symmetric skyrmion collapse. Cones mark the magnetization directions $\boldsymbol{m}$ for each atom. The color indicates the z component of the magnetization m_z. Inset number indicates the displacement along the minimum energy path, i.e. the reaction coordinate of (b). **d**, Maps of topological charge per triangle A_i (methods) along the same GNEB minimum energy path. **e, f**, Same as (c),(d) for the chimera collapse. More details on both mechanisms are shown in Supplementary Figs. S11-S12 and movies 1-2.

[40] and transition state theory [41] (methods). We experimentally tune the collapse mechanism and rate by both, in plane and out-of-plane fields (Fig. 1a), changing the rate by up to four orders of magnitude. We also establish that both collapse mechanisms are induced by the local energy injection of a single hot electron with tunneling energy $eV \gg k_\text{B}T$ (T: temperature, k_B: Boltzmann constant).

TWO SKYRMION COLLAPSE MODES

Figure 1a sketches the experimental STM setup to map magnetic skyrmions in a biatomic Pd/Fe bilayer, fcc stacked on Ir(111). Depending on the applied in-plane, $B_\parallel$, and out-of-plane, $B_\perp$, magnetic fields, the skyrmion collapses via the radial symmetric or the chimera-type mechanism (Fig. 1b). Spin configurations along the minimum energy path of the usual radial symmetric collapse, obtained via the GNEB method, are shown in Fig. 1c (more details: Supplementary movies). The spin structure exhibits the well-known shrinkage of the area with spins that are not oriented along $B_\perp$ [40, 42]. At the saddle point (SP), i.e. the image at the energy barrier along the reaction coordinate (Fig. 1b), three central spins point towards each other representing the topology flip. Indeed, maps of the topological charge density $\rho_{\text{topo}} = \frac{1}{4\pi}\boldsymbol{m}\cdot(\partial_x\boldsymbol{m}\times\partial_y\boldsymbol{m})$ ($\boldsymbol{m} = \boldsymbol{M}/M$: normalized magnetization), as realized on a discrete lattice via the topological charge per triangle A_i (methods), exhibit an initial shrinkage towards this point up to the SP (Fig. 1d). Afterwards, the central part of ρ_{topo} reverses sign accompanied by the sign change of the z component of $\boldsymbol{m}$, m_z, in the skyrmion center, before annihilating with its surrounding. The energy along the minimum energy path exhibits a maximum at the topology flip (Fig. 1b).

The minimum energy path of the chimera process is displayed in Fig. 1e. In contrast to the radial symmetric collapse, the spin structure at the SP has barely shrunk. Instead, the spins opposing $B_\parallel$ have rotated in out-of-plane direction with the spins in the inner and the outer skyrmion area pointing oppositely. This gives rise to a Bloch-like point at the left foreground of the SP image in (e), such that the canting between neighboring spins is strongly anisotropic. Subsequently, some spins of this area rotate their in-plane direction and, thus, annihilate the Bloch-like point. This introduces an area of opposing ρ_{topo} that exactly cancels with the remaining topological charge of the rest of the spin structure, such that the total topological charge switches to zero (Fig. 1b). Afterwards, the spin structure does not require further spin flips while continuously rotating until being fully aligned with $B_\perp$.

The barrier height of the two collapse mechanisms is similar at the chosen magnetic fields, while the shape of the minimum energy path is different (Fig. 1b). The shrinking of the skyrmion during the radial symmetric collapse continuously costs energy, while the chimera mode exhibits a lateral movement of the skyrmion center during the first part of the reaction path that barely requires energy. It is followed by a sharp energy maximum around the SP and a subsequent plateau marking the continuous spin rotation of the vanishing spin texture after annihilating the Bloch like point. While the out-of-plane spin flip at the SP of the radial collapse is assisted

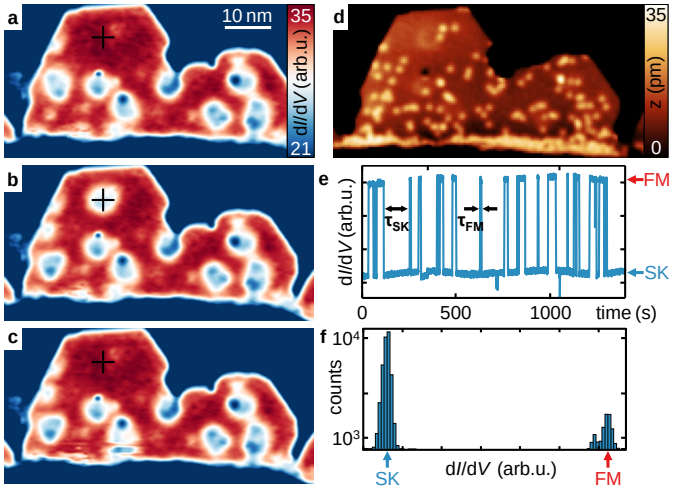

Figure 2. **Current induced skyrmion switching (Pd/Fe/Ir(111)). a-c**, Subsequently recorded dI/dV maps of the same area featuring the creation ((a) → (b)) and annihilation ((b) → (c)) of a single skyrmion, $I = 300\,\mathrm{pA}$, $V = 610\,\mathrm{mV}$. Between the images, that each last about 10 min, the tip is positioned at the marked cross and the current is raised to 10 nA until a switching event is observed via a spontaneous current change (e). Afterwards the current is reduced immediately to 300 pA for imaging. **d**, Topographic image recorded simultaneously with (b). The skyrmion is faintly visible as a ring contrast via NCMR that probes the areas of strongest spin canting (methods). **e**, Time trace of dI/dV signal recorded at the position indicated by a cross in (a)-(c), $I = 10\,\mathrm{nA}$, $V = 610\,\mathrm{mV}$. Two individual life times of skyrmion state (τ_{SK}) and ferromagnetic state (τ_{FM}) are marked. **f**, Histogram of dI/dV values from the time trace with $\Delta t = 1430\,\mathrm{s}$, shown in (e), and exhibiting two distinct peaks that represent the skyrmion (SK) and the ferromagnetic (FM) state. (More time traces and histograms: Extended Data Fig. 3) **a-f** $B_{\parallel} = 0\,\mathrm{T}$, $B_{\perp} = 1.5\,\mathrm{T}$, $T = 6\,\mathrm{K}$.

by $B_{\perp}$, the in-plane spin flip at the SP of the chimera mode is favored by $B_{\parallel}$. Thus, a transition between the two mechanisms is expected by tuning the relation of $B_{\parallel}$ and $B_{\perp}$ as indeed revealed by a detailed analysis of the energy contributions (Supplementary sections S8/S9).

MAPPING SKYRMION COLLAPSE RATES

Figure 2 introduces the experimental access to the collapse mechanisms via mapping the skyrmion flip rate. Figure 2a-c show the same area several times as recorded by SP-STM at $B_{\perp} = 1.5\,\mathrm{T}$. A number of skyrmions is visible as roughly circular contrasts with rich internal structure. The contrast is caused by a spin-polarized contribution to the tunnel current due to the magnetic tip [39, 43] and an electronic contribution due to the noncollinear arrangement of spins coined the non-collinear magnetoresistance (NCMR) [23] (methods). The sequence of three images (Fig. 2a-c) showcases the presence and absence of one skyrmion as marked by a cross. This skyrmion covers an area of reduced defect density (Fig. 2d), while all other, more stable skyrmions are accompanied by several defects implying that defects enhance the skyrmion stability. The defects are related to Fe atoms within the Pd layer [32] that pin skyrmions excentrically according to DFT based theory [44] as in the experiment. Such defects are not considered in our calculations in order to reduce complexity. Hence, we carefully select defect free skyrmions in experiment for later comparison with theory. Importantly, the switching rate of the nearly free skyrmion (cross in Fig. 2a-c) increases with increasing tunnel current I. This leads to telegraph noise at larger I (Fig. 2e), i.e., the dI/dV signal flips between two values representing the skyrmion and the ferromagnetic state (Fig. 2f). In Fig. 2e, we have choosen a voltage and position within the skyrmion that exhibits maximum contrast between the two states prior to probing the telegraph noise. By immediately reducing I at the lower (higher) dI/dV value, the created skyrmion (ferromagnetic) state can be mapped (Fig. 2a-c).

We use this telegraph noise to determine the flip rate of the skyrmion as function of current injection point by the tip. This leads to two flip rate maps for creation and collapse of the skyrmion, respectively. Figure 3 e-h show the collapse rate maps at different $\boldsymbol{B}$ in comparison with the dI/dV maps of the same skyrmion probed at low I (Fig. 3a-d). Maps of the corresponding creation rates are largely homogeneous within the skyrmion area (Extended Data Fig. 1, Supplementary section S1). Most intriguingly, the maps of the collapse rate exhibit a hot spot within the area of the skyrmion, i.e., a small area with markedly increased rate (profile lines in Fig. 3i-l). This hot spot is located in the center of the skyrmion at $B_{\parallel} = 0\,\mathrm{T}$ (Fig. 3e) and strongly displaced sidewards at finite $B_{\parallel}$ along the $B_{\parallel}$ direction (Fig. 3b-d). The displacement direction flips sign by changing either the sign of $B_{\perp}$ (Fig. 3f → g) or the sign of $B_{\parallel}$ (Fig. 3g → h). Comparison with the dI/dV maps (Fig. 3a−d) reveals that the hot spot is always located close to the area of smallest dI/dV (see also profile lines, Fig. 3i-l), marking the area of strongest spin canting between neighboring spins via the dominating NCMR contrast (methods). The collapse is, hence, strongly favored by injecting electrons at the area of strongest spin canting, where spin flips are easier due to the initially strong exchange energy density. This area of strong spin canting is markedly displaced from the skyrmion center at finite $B_{\parallel}$ (Extended Data Fig. 2e-h), while the out-of-plane spins opposing $B_{\perp}$ are still located close to the center (Fig. 4b, Extended Data Figs. 2j-l, 6a). Inverting the direction of either $B_{\perp}$ or $B_{\parallel}$ switches the position of strongest relative spin canting with respect to the skyrmion center and, consistently, we observe a position switch of the hot spot in the skyrmion collapse rate. Interestingly, the central hot spot at $B_{\parallel} = 0\,\mathrm{T}$ (Fig. 3e, i) is accompanied by a side arm that points towards the left rim of the island (skyrmion A in Fig. 6a, Supplementary section S4).

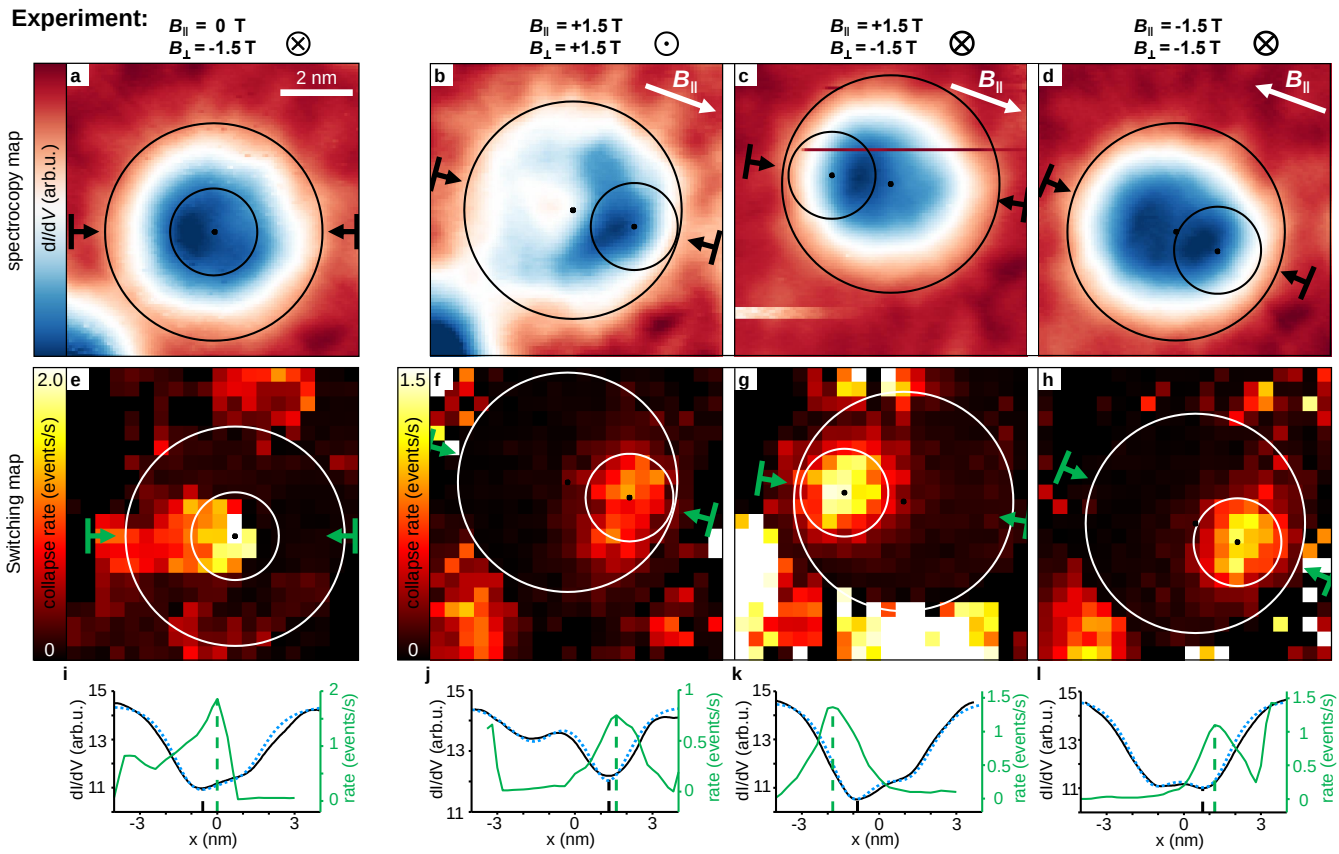

Figure 3. **Maps of skyrmion collapse rate in Pd/Fe/Ir(111). a-d**, Experimental dI/dV maps of the same skyrmion at different magnetic fields $\boldsymbol{B}$ as indicated above the images, $I = 1\,\mathrm{nA}$, $V = 610\,\mathrm{mV}$. The direction of $B_\parallel$ is marked. The larger circle encloses the skyrmion area with radius $r = 3\,\mathrm{nm}$ as deduced by adapting the dI/dV contrast to the spin canting of the simulation such that the spins on the circle are canted by 10° relative to the out-of-plane direction (methods). The smaller circle with radius $r = 1.2\,\mathrm{nm}$ encloses the area of increased collapse rate as determined in (e)−(h). Black dots mark the center of the circles. Black arrows indicate the orientation of profile lines displayed in (i)-(l). **e-h** Experimental maps of the skyrmion collapse rate corresponding to the dI/dV maps above. Each pixel (20 × 20 per map) results from a time trace of 400 s at $I = 600\,\mathrm{nA}$ (e) and 150 s at $I = 60\,\mathrm{nA}$ (f), $I = 50\,\mathrm{nA}$ (g) and $I = 55\,\mathrm{nA}$ (h). Circles have identical radius and position as in (a)-(d) with the smaller circle roughly marking the full width at half maximum of the hot spot. Arrows are at identical positions as in (a)-(d), too, and mark the directions of profile lines in (i)-(l). **i-l**, Profile lines of collapse rate (green) and dI/dV contrast (black) along the directions marked by arrows in (a)-(h). The blue dotted lines are dI/dV profiles of skyrmions as calculated from the spin textures of the DFT based atomistic spin simulations (Fig. 4, Extended Data Fig. 2). All profiles are averaged across 1 nm (widths marked by the thicker bars perpendicular to the arrows in (a)-(h)). Dashed vertical lines mark maximum (minimum) of the green (black) curve highlighting a small, but systematic mutual offset. (Collapse and creation rate maps of another skyrmion: Extended Data Fig. 1)

CALCULATING SKYRMION COLLAPSE PATHS

In order to rationalize the experimental observations, we perform minimum energy path simulations based on an atomistic spin model parametrized from DFT calculations for Pd/Fe/Ir(111) (methods). The minimum energy paths reveal which spins need to be activated to lift the skyrmion across the energy barrier and, hence, to trigger the collapse. The positions of those most active spins are compared with the location of the measured hot spots of skyrmion collapse rates, thereby providing the interpretation of the experiment.

Figure 4e-j illustrates the transition state of the skyrmion collapse without and with $B_\parallel$. We use the skyrmion radius as benchmark for the comparison with the experiment to adapt $B_\perp$ [35], deduced by matching measured and simulated dI/dV profile lines (Fig. 3(i)−(l)), eventually implying $B_\perp = 3.2$ T in the simulations (methods). The spin structure of the skyrmion state is only little affected by $B_\parallel$ (Fig. 4a,b). However, in agreement with experiment (Fig. 3a,b), the simulated SP-STM images (Fig. 4c,d) exhibit a strong asymmetry due to the anisotropic canting angle of neighboring spins as probed by the dominating NCMR (methods).

Without $B_\parallel$, the calculated skyrmion collapse is radially symmetric via a shrunk spin texture at the SP (Fig. 4g). The energy density map at the SP (to-

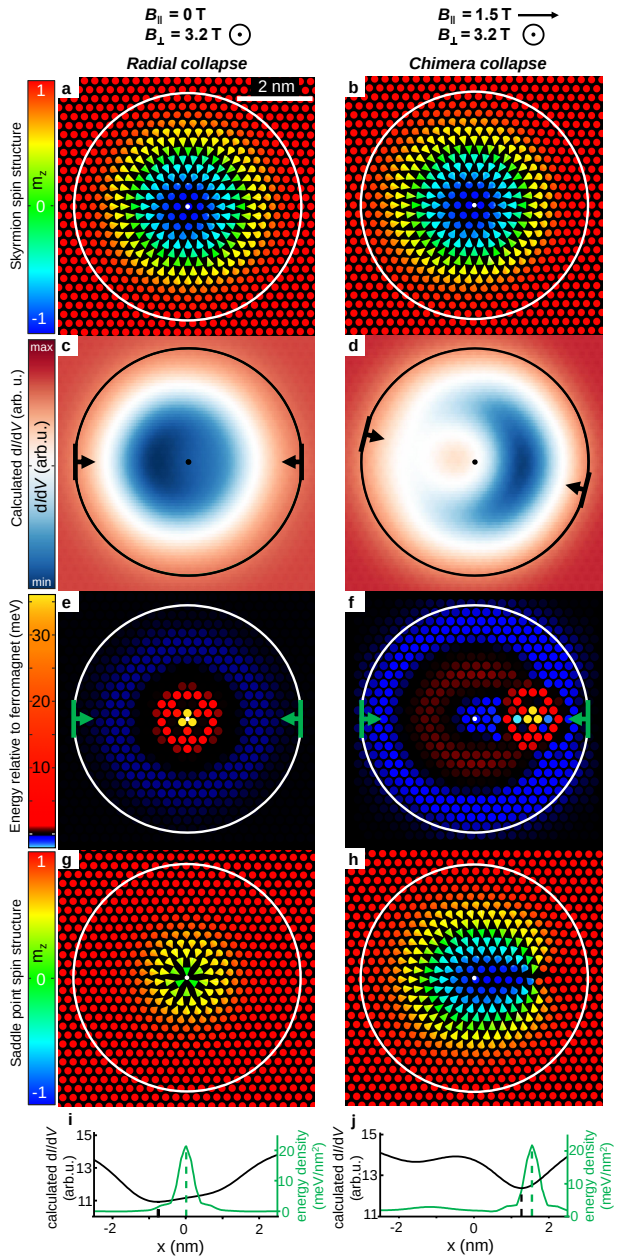

Figure 4. **Simulated skyrmion collapses in Pd/Fe/Ir(111). a,b**, Spin structure of the relaxed skyrmion state at $B_\perp = 3.2\,\mathrm{T}$, (a) $B_\parallel = 0\,\mathrm{T}$, (b) $B_\parallel = 1.5\,\mathrm{T}$. **c,d**, Simulated dI/dV maps of the spin structures shown in (a)−(b) matching the experimental dI/dV maps (Fig 3a-b) via adapted NCMR contrast and tunneling magnetoresistance (methods). **e,f**, Calculated energy density maps at the saddle point (SP) of the radial symmetric (e) and chimera (f) collapse. Arrows in (c)−(f) mark directions and interpolation widths of profile lines shown in (i)−(j). **g,h**, Spin structures at SP for the radial (g) and the chimera (h) collapse. Circles in (a)−(h) have the same size ($r = 3\,\mathrm{nm}$) identical to the larger circles in Fig. 3(a)−(h). **i**, Profile lines along arrows in (c), (e), i.e., for the radial collapse. **j**, same profile lines for (d), (f), i.e., for the chimera collapse. Black lines are again plotted as blue dotted lines in Fig. 3(i)−(j). Dashed lines mark maximum (minimum) of the green (black) curve for comparison with Fig. 3(i)−(j).

tal energy per atom with respect to the ferromagnetic state) is radially symmetric with maximum at the center (Fig. 4e). This illustrates the increased exchange energy by strong relative canting of the central spins. An energy gain on a ring around the center is also visible due to the stronger rotation of neighboring spins gaining Dzyaloshinskii-Moriya interaction relative to the ferromagnetic state (Extended Data Fig. 5). At finite $B_\parallel$, the chimera collapse becomes favorable showcasing an asymmetric spin configuration at the SP with Bloch-like point at the right circumference (Fig. 4h). The size of the skyrmion barely changes up to the SP. The energy density map (Fig. 4f) is asymmetric with a maximum at the Bloch-like point due to the increased exchange energy there.

Intriguingly, the hot spots of the calculated energy density maps at the SP (Fig. 4e,f) match the measured hot spots of the skyrmion collapse rates (Fig. 3e,f) nicely. This is our central result that experimentally demonstrates a transition from the radial symmetric to the chimera-type collapse with increasing $B_\parallel$. Extended Data Fig. 6 reveals that the radial collapse at finite $B_\parallel$ still has the hot spot of SP energy density close to the center of the skyrmion.

COMPARING COLLAPSE RATES

In the following, we will substantiate this central result by comparing the collapse rates between experiment and theory quantitatively and by providing a tentative model of the skyrmion collapse via a single hot electron process. Oerstedt fields of the tunnel current amount to μT [45] and are, thus, negligible.

Theoretically, we obtain the collapse rates ν within quasi-equilibrium implying an Arrhenius law at fixed T:

$$\nu = \nu_0 \exp\left(-\frac{\Delta E}{k_\mathrm{B} T}\right). \qquad (1)$$

Here, ν_0 is the attempt frequency, also called prefactor, and ΔE is the energy barrier. Both quantities depend on the mechanism of skyrmion collapse and are calculated within harmonic approximation to the rate theory (methods) as a function of $B_\parallel$ for various $B_\perp$ (Fig. 5). At $B_\perp = 3.2\,\mathrm{T}$ (Fig. 5a), the radial collapse mechanism occurs only up to $B_\parallel < 0.3$ T and exhibits a higher energy barrier (black circles) than the chimera collapse (black dots). The chimera collapse occurs at all $B_\parallel$ with energy barriers decreasing with increasing $B_\parallel$ due to the increased in-plane Zeeman energy gain of spins along $B_\parallel$ at the SP (Supplementary section S9). The prefactor of the chimera collapse (blue dots, Fig. 5a) decreases with $B_\parallel$, too, and is similar in magnitude to the prefactor of the radial collapse (blue circles) at low $B_\parallel$. At $B_\perp = 4.0\,\mathrm{T}$ (Fig. 5b), the radial collapse is stable up to $B_\parallel = 1\,\mathrm{T}$ with energy barriers partially lower than for the chimera mode. The prefactor of both mechanisms increases towards the energetic crossover due to mode softening that

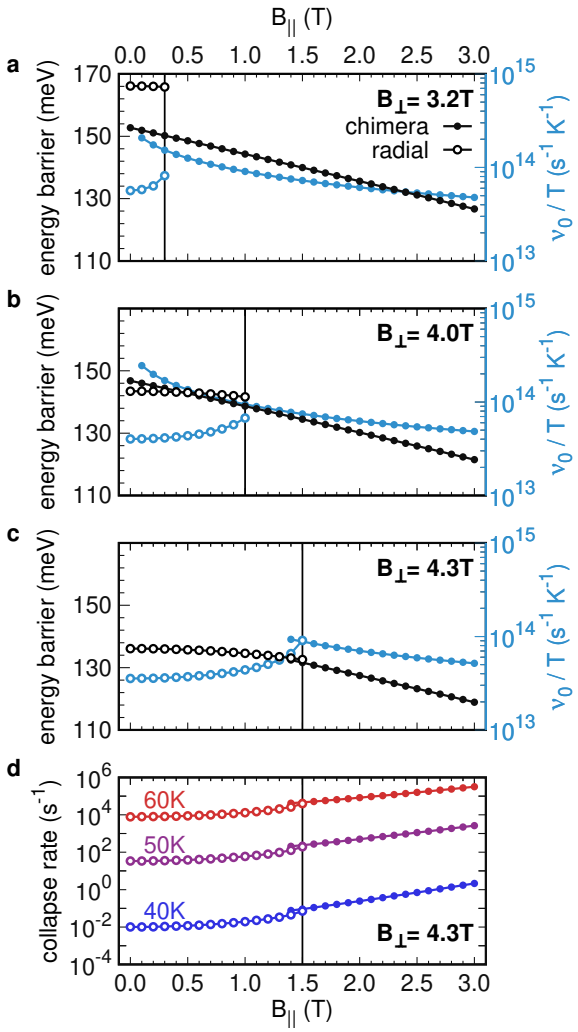

Figure 5. **Calculated energy barriers and prefactors for skyrmion collapse (Pd/Fe/Ir(111)). a-c**, Energy barriers (black) and prefactors divided by temperature, ν_0/T (blue), for the radial symmetric (open symbols) and chimera collapse (full symbols) of an isolated skyrmion at varying $B_\parallel$ according to atomistic spin simulations via GNEB and transition state theory based on parameters from DFT (methods). (a) $B_\perp = 3.2\,\mathrm{T}$, (b) $B_\perp = 4.0\,\mathrm{T}$, (c) $B_\perp = 4.3\,\mathrm{T}$. **d**, Thermal collapse rates resulting from (c) using eq. (1) for three temperatures with filled (open) circles employing the chimera (radial symmetric) collapse. Vertical lines in (a)−(d) mark the maximum $B_\parallel$, at which the radial symmetric collapse could be stabilized via GNEB.

increases the entropy of the transition states [46]. Far from the crossover, the prefactors of both mechanisms approach a similar value. At even higher $B_\perp = 4.3\,\mathrm{T}$ (Fig. 5c), the radial symmetric collapse is favorable up to $B_\parallel = 1.5\,\mathrm{T}$, where the chimera collapse is unstable, while the opposite is true at larger $B_\parallel$.

These results demonstrate consistently that the symmetric collapse is favored by $B_\perp$, while $B_\parallel$ supports the chimera-type mechanism. This is caused by the favorable influence of Zeeman energy at the SP along $B_\perp$ and along $B_\parallel$, respectively. (Supplementary sections S8/S9). Based on the calculated prefactors and energy barriers, eq.(1) provides collapse rates $\nu(B_\parallel)$ at different T as shown for $B_\perp = 4.3\,\mathrm{T}$ (Fig. 5d). As expected, the rate increases drastically with T and rises with $B_\parallel$ exhibiting a transition from preferential radial collapse to preferential chimera-type collapse for $B_\parallel \simeq 1.5$ T.

Experimentally, we obtain the trend of skyrmion collapse rates with $B_\parallel$ by measuring the random telegraph noise within the central skyrmion area. Again, we select a visibly defect-free skyrmion (skyrmion A in Fig. 6a,b) and compare it to another skyrmion B that exhibits two defects within its area that pin the skyrmion [32]. Generally, we found that the defect configuration influences the collapse rate and the transition rate map (not shown), such that the selection of a rather defect free skyrmion is crucial for the comparison with the theoretical results. Firstly, we show that the skyrmion collapse and creation are single electron processes, i.e., the corresponding switch rates scale linearly with I (Fig. 6c). This applies for, both, skyrmion collapse and creation at all studied magnetic fields (Fig. 6d−e), hence, enabling to deduce a probability for collapse and creation per injected electron (Fig. 6f-g). The resulting collapse probability P_{collapse} increases by two orders of magnitude with $B_\parallel$ for the defect-free skyrmion A (Fig. 6f), prior to skyrmion disappearance at larger $B_\parallel$. This fits nicely with the change in collapse rate by about two orders of magnitude found theoretically at constant T (Fig. 5d). The pinned skyrmion B is stable up to larger $B_\parallel$ and its $P_{\mathrm{collapse}}(B_\parallel)$ covers even four orders of magnitude. Moreover, $P_{\mathrm{collapse}}(B_\parallel)$ is significantly steeper for skyrmion B, highlighting the importance of defects that tend to stabilize skyrmions in Pd/Fe/Ir(111) [44] as corroborated by probing multiple skyrmions on that surface. In contrast, the creation probability (Fig. 6g) barely depends on $B_\parallel$ as also found theoretically via the atomistic spin simulations (Extended Fig. 7d). It also barely depends on the defect configuration.

Eventually, we compare the measured $P_{\mathrm{collapse}}(B_\parallel)$ (Fig. 6f) with the calculated collapse rates at constant T. For this purpose, we use a simplified model assuming that each electron heats a certain area of the skyrmion for a short time such that the collapse can proceed via eq. 1 (justification: Supplementary section S7). We employ a finite element calculation for a semi-infinite crystal and initially deposit the energy of a single hot electron in a small circle (radius: 0.25 nm) at the surface. Subsequently, we calculate the 3D propagation of T as function of time t using heat capacitance $c_p(T)$ and heat conductivity $\kappa(T)$ of Pd (methods, inset of Fig. 6h). Figure 6h displays the resulting spatially averaged $T(t)$ for different circular areas at the surface, namely the area of energy deposition ($r = 0.25\,\mathrm{nm}$), the area of the skyrmion ($r = 3.0\,\mathrm{nm}$), the area of the hot spot for collapse ($r = 1.2\,\mathrm{nm}$, Fig. 3) and a radius in between ($r = 1.7\,\mathrm{nm}$).

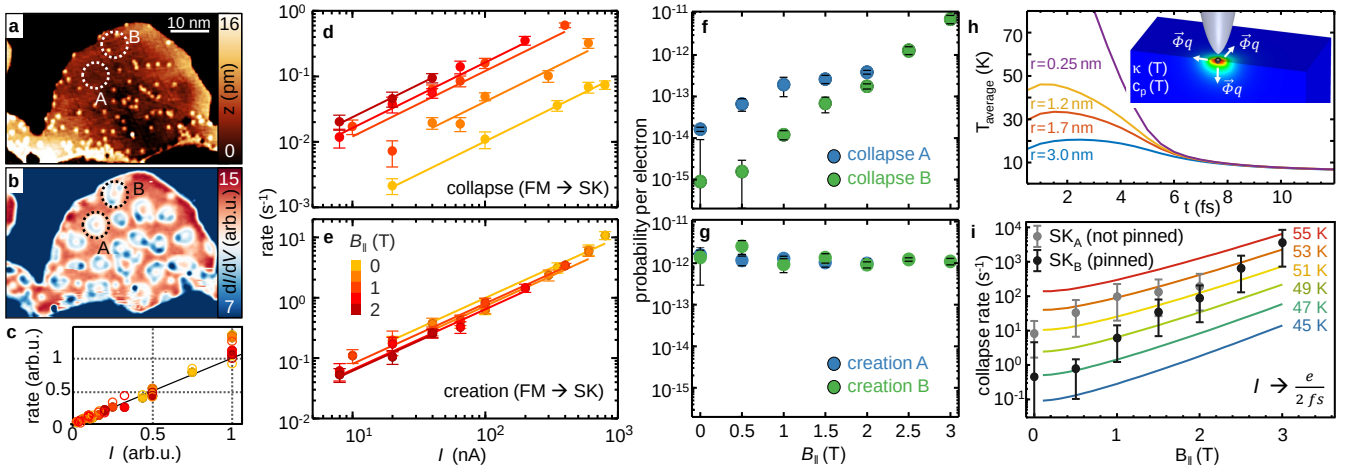

Figure 6. **Skyrmion collapse and creation rates at different $B_\parallel$ (Pd/Fe/Ir(111)).** **a** STM topography of a Pd island on Fe/Ir(111) with the two investigated skyrmions encircled, $B_\parallel = 0\,\mathrm{T}$, $B_\perp = 1\,\mathrm{T}$, $V = 610\,\mathrm{mV}$, $I = 2\,\mathrm{nA}$. **b** Simultaneously recorded dI/dV map with the same skyrmions encircled and labeled as in (a). **c** Collapse rates (circles) and creation rates (dots) as function of tunnel current I at different $B_\parallel$ (color code as in (e)). Both, I and rate ν are linearly scaled to exhibit the same slope $\Delta\nu/\Delta I$ of the linear fit curve to the data to display all data within a single graph. The linearity implies that the collapse is induced by independent single electron events. **d** Collapse rate of skyrmion A as function of I in log-log scale at different $B_\parallel$ marked via symbol colors according to legend in (e), $V = 610\,\mathrm{mV}$, $B_\perp = 1.5\,\mathrm{T}$. Linear fit lines are added in identical color. **e**, Creation rate of skyrmion A at the same parameters as in (d). **f, g**, Probability per electron of skyrmion collapse (f) and creation (g) as deduced from linear fits of (d), (e) for the two skyrmions marked in (a), (b), $B_\perp = 1.5\,\mathrm{T}$, $V = 610\,\mathrm{mV}$. **h** Simulated temporal development of mean temperature within a surface area of radius r, after inducing the energy of a single electron ($V = 610$ mV) homogeneously within $r = 0.25\,\mathrm{nm}$ at $t = 0\,\mathrm{fs}$. Inset: Sketch of the finite element model with indicated heat flow $\vec{\Phi}_q$, heat conductivity $\kappa(T)$, and heat capacitance $c_p(T)$. **i** Calculated thermal collapse rates at different T using the theoretical parameters from Fig. 5a (colored lines) and corresponding experimental collapse rates (symbols) extrapolated from the single electron probabilities (f) and assuming $I = e/2\,\mathrm{fs} = 75\mu\mathrm{A}$ such that the area of $r = 1.2\,\mathrm{nm}$ (hot spot in Fig. 3) would be continuously heated to about 45 K according to the calculation of (h) (Supplementary section S7, comparison of creation rates: Extended Data Fig. 8). Error bars in (d), (e) indicate the 95% confidence interval of the maximum likelihood estimate deduced from time traces (methods). Error bars in (f), (g) indicate the 95% confidence interval of the weighted linear fits of the data in (d), (e). Error bars in (i) result from the uncertainty of the adaption of I to a continuous T via (h).

The whole skyrmion (hot spot) is heated by each electron up to about 20 K (45 K) for a few fs. This time is much shorter than the average time τ between sequentially tunneling electrons $\tau = e/I \geq 150\,\mathrm{fs}$ (e: electron charge). Such time scale mismatch straightforwardly explains the deduced single electron processes, i.e., the skyrmion is always cooled down prior to the next electron injection. An estimate of the heat induced dynamics is given by considering the hot spot area to be at $T \simeq 45\,\mathrm{K}$ for $\Delta t \simeq 2\,\mathrm{fs}$ after injecting the electron, respectively, the whole skyrmion area at $T \simeq 20\,\mathrm{K}$ for $\Delta t \simeq 4\,\mathrm{fs}$ (details: Supplementary section S7).

In turn, a continuously increased T within these areas implies a current $I = e/\Delta t$ via independent, subsequent electrons. Accordingly, we scale the experimental $P_{\mathrm{collapse}}(B_\parallel)$ to collapse rates $\nu(B_\parallel) = P_{\mathrm{collapse}}(B_\parallel)/\Delta t$ that would realize quasi-constant T. The resulting $\nu(B_\parallel)$ are then straightforwardly compared to the theoretically deduced rates using eq. (1) with parameters from Fig. 5a at different T. Figure 6i provides such comparison for $\Delta t = 2\,\mathrm{fs}$. Intriguingly, the experimental data of the defect-free skyrmion A (grey symbols) match the theoretical data for $T \simeq 50\,\mathrm{K}$, very close to the estimated average temperature of the hot spot $T \simeq 45\,\mathrm{K}$.

Thus, shortly heating the hot spot via a single hot electron to 50 K appears to be the central ingredient to the skyrmion collapse. The additional spin torque of each hot electron sincerely contributes, but this influence is less crucial, i.e., mostly part of the Arrhenius type statistics. Doubling Δt, i.e., adapting the scaled I in Fig. 6i towards heating the whole skyrmion to a continuous temperature, does not significantly change the required $T \simeq 50\,\mathrm{K}$ for matching theory. Consequently, heating the hot spot is more crucial than heating the whole skyrmion that only achieves $T \simeq 20\,\mathrm{K}$.

This straightforwardly implies that the rate must significantly increase, if the hot electron hits the hot spot of energy density at the SP directly, hence, explaining the observed hot spots in the collapse rate maps of Fig. 3. The very good agreement of temperatures between theory and experiment strongly corroborates our interpretation that the measured off-center hot spot in the collapse rate is linked to the calculated hot spot in SP energy density of the chimera collapse. Moreover, the single hot electron mechanism explains why previous Monte-Carlo simulations had to assume $T = 80\,\mathrm{K}$ to fit experimental

collapse data observed at $T = 4\,\mathrm{K}$ [31].

CONCLUSIONS AND OUTLOOK

Mapping transition rates that are initiated by local energy deposition on the sub-nm scale enabled us to determine the typically elusive *transient state* that, so far, has been inferred from parameter-based simulations only. The resulting detailed understanding of the skyrmion stability is a crucial ingredient to prohibit its annihilation [3, 6, 8], but can also be employed to design intentional deleting of skyrmions via the strong dependence of the collapse rate on $B_\parallel$. While avoiding $B_\parallel$, consisting of external and internal fields, improves the stability of skyrmions by prohibiting the chimera collapse, the opposite can be used to deliberately delete individual skyrmions, e.g., via placing micromagnets along the track. Hence, our experimental access to transient states provides novel design criteria for exploitation of the prospective magnetic skyrmions.

I. METHODS

Preparation of Pd/Fe bilayer. The Ir(111) crystal was cleaned in ultrahigh vacuum at base pressure $10^{-10}\,\mathrm{mbar}$ by repeated cycles of annealing up to 1200 K in oxygen at decreasing partial pressure from $10^{-6}\,\mathrm{mbar}$ to $10^{-8}\,\mathrm{mbar}$. Additionally, cycles of argon ion bombardment at room temperature followed by flash annealing to 1700 K were performed. Subsequently, a Fe monolayer was deposited by electron beam evaporation at sample temperature 470 K implying step-flow growth. Finally, we evaporated Pd using electron beam evaporation at substrate temperature of 400 K, resulting in separated islands covering about 50 % of the surface. For all presented measurements, we selected fcc stacked islands via their characteristic dI/dV spectra [47] (Supplementary section S5).

Spin polarized STM. The tunneling tip, fabricated from a $0.5 \times 0.5\,\mathrm{mm}^2$ beam of polycrystalline, antiferromagnetic Cr (purity 99.99+%), exhibits a final spin-polarized Cr atom at the apex acting as spin filter for spin-polarized STM [48]. These tips have the advantage of a strongly reduced stray field such that the probed magnetic textures are barely disturbed. Tip sharpening employs electrochemical etching by a 2.5 M NaOH film suspended within a PtIr loop at 5.5 V with respect to the tip. Etching is stopped at drop off of the lower beam part via differential current detection. The upper part of the beam is immediately rinsed with deionized water and glued onto a custom-made tip holder. The tip is then loaded into ultrahigh vacuum and, subsequently, into the STM scan head at 6 K [49]. The atomic tip structure is optimized during tunneling by voltage pulses (10 V/30 ms) until spin contrast is achieved. Voltage V is applied to the sample. The differential conductance $\mathrm{d}I/\mathrm{d}V$ is measured by adding a 50 mV RMS sinusoidal voltage (1384 Hz) to the DC voltage and recording the resulting oscillation amplitude of the tunnel current I via lock-in amplifier. The system provides a 3D magnetic field $\boldsymbol{B} = (B_x, B_y, B_\perp)$ with out-of-plane component $B_\perp$ up to 7 T and simultaneous in-plane part $\boldsymbol{B}_\parallel = (B_x, B_y)$ up to 0.5 T in each in-plane direction and up to 3 T in a single direction [49]. We applied $B_\parallel$ along the single direction determined precisely by the induced movement of magnetic vortex cores [50] and marked in Fig. 3b–d.

Determining switching rates. To determine the switching rate maps as displayed in Fig. 3e–h, we use time traces of dI/dV, $dI/dV(t)$, recorded at each position in constant-current mode (Fig. 2e, Extended Data Fig. 3). Such time traces last $150 - 400\,\mathrm{s}$ at each position of the map. For each $dI/dV(t)$, we determine all τ_{SK} and τ_{FM} as dwell times of the corresponding level after binning. We employ the time derivative of $dI/dV(t)$ to identify switching events as spikes that are additionally verified as such by distinct values of the time-averaged dI/dV between the switching events. These values are mostly below the 5 % percentile and above the 95 % percentile of the dI/dV distribution for τ_{SK} and τ_{FM}, respectively (Supplementary Section S3). The collapse (creation) rate λ_{SK} (λ_{FM}) for a time trace is then calculated as the inverse of the average of the observed τ_{SK} (τ_{FM}) dubbed $\overline{\tau}_{\mathrm{SK}}$ ($\overline{\tau}_{\mathrm{FM}}$). The skyrmion probability of the time trace reads:

$$P_{\mathrm{SK}} = \frac{\overline{\tau}_{\mathrm{SK}}}{\overline{\tau}_{\mathrm{SK}} + \overline{\tau}_{\mathrm{FM}}}. \tag{2}$$

Graphs of collapse (creation) rates as function of current I at different $B_\parallel$ (Fig. 6c–e) are based on time traces lasting several 100 s. The resulting rates are determined via the maximum likelihood estimator of the exponential distribution of τ_{SK} and τ_{FM}. This enables to deal with the time resolution of the experiment (25 ms), i.e., we could measure only dwell times larger than 25 ms. As usual for telegraph noise, we assume an exponential probability distribution of the dwell times mimicking a Poisson point process, $P(\tau_{\mathrm{SK}})$, reading

$$P(\tau_{\mathrm{SK}}) = \overline{\tau}_{\mathrm{SK}}^{-1} \cdot \exp\left(-\frac{\tau_{\mathrm{SK}}}{\overline{\tau}_{\mathrm{SK}}}\right), \tag{3}$$

and correspondingly for $P(\tau_{\mathrm{FM}})$ (Supplementary Fig. S2). To determine the average rates $\overline{\tau}_{\mathrm{SK}}^{-1}$, respectively $\overline{\tau}_{\mathrm{FM}}^{-1}$, we use the left truncated maximum likely-hood estimator to adapt $P(\tau_{\mathrm{SK}})$, respectively $P(\tau_{\mathrm{FM}})$. Error bars indicate the 95% confidence interval of the maximum likelihood estimate for the resulting average rates $\overline{\tau}_{\mathrm{SK}}^{-1}$ and $\overline{\tau}_{\mathrm{FM}}^{-1}$.
Subsequently, we perform weighted linear fits to the deduced average rates as function of I for each $B_\parallel$ (Fig. 6d–e). This returns the switching probability per electron as function of $B_\parallel$ (Fig. 6f–g) with error bars indicating the 95% confidence intervals of the weighted linear fits.

The error bars of the eventually deduced collapse rates at quasi-constant temperature T (Fig. 6i) are goverened by the uncertainty in required current to achieve this quasi-constant T (Supplementary Section S7).

Atomistic spin model. The atomistic spin dynamics, GNEB, and transition state theory calculations are performed in a simulation box of a hexagonal 70 × 70 atomic lattice with periodic boundary conditions. The applied extended Heisenberg Hamiltonian reads

$$\mathcal{H} = -\sum_{ij} J_{ij}\Big(\mathbf{m}_i \cdot \mathbf{m}_j\Big) - \sum_{ij} \mathbf{D}_{ij}\Big(\mathbf{m}_i \times \mathbf{m}_j\Big) + K\sum_i \Big(\mathbf{m}_i^z\Big)^2 - M\sum_i \Big(\mathbf{m}_i \cdot \mathbf{B}_{\text{ext}}\Big) \quad (4)$$

Here, $\mathbf{m}_i = \frac{\mathbf{M}_i}{M}$ is the normalized vector of the magnetic moment of the atom at the lattice site i. The parameters J_{ij} and the vectors $\mathbf{D}_{ij}$ denote the strength of the exchange interaction and the strength and rotational sense of the Dzyaloshinskii-Moriya interaction between the spins at i and j, respectively. The strength of the uniaxial magnetocrystalline anisotropy in out-of-plane direction is given by the parameter K, while the external magnetic field $\mathbf{B}_{\text{ext}}$ enters the Zeeman interaction. All parameters of eq. (4) including the magnetic moment M are based on DFT calculations for fcc-Pd/fcc-Fe/Ir(111) as taken from Ref. [35]. The atomistic spin model is applicable, since the Fe magnetic moments are large ($\approx 2.65\ \mu_B$), localized, and longitudinal fluctuations of the magnetic moments are very small. In DFT calculations of spin spirals, we find a variation of the moments of less than 5% over the full range of the spin spiral vector [51, 52]. The applicability of the atomistic spin model with DFT parameters is supported by the good agreement of the obtained skyrmion properties to experimental data [35, 43], most strikingly, if comparing the B-T phase diagram obtained from Monte-Carlo simulations, that are based on our DFT parameters [53], with the phase diagram determined experimentally using STM [54].

Selection of $B_\perp$ in the simulations and extraction of skyrmion radius using dI/dV maps. The DFT calculations provide a good quantitative description of the magnetic interactions for Pd/Fe/Ir(111) [35], as seen e.g. from the extracted effective interaction parameters [35] that are favorably compared with experimental data [43]. In particular, the frustration of exchange interactions is captured being important for the chimera collapse [25, 55]. However, there are deviations concerning $\mathbf{B}$ due to the relatively small Zeeman energy, i.e., the phase transitions between the spin spiral, the skyrmion lattice, and the ferromagnetic state are shifted with respect to experiments [35]. Most importantly, a magnetic field of 1 T corresponds to a Zeeman energy of 0.2 meV per Fe atom only. This is more than an order of magnitude smaller than the effective exchange energy and similar to the depth of the energy minima of spin spirals as a function of wave vector [35]. Hence, a subtle interplay of energy scales governs the $\mathbf{B}$ dependence of skyrmion properties. It is strongly influenced by minor deviations of exchange energies between theory and experiment. Since we found that the main contribution changing the preferential collapse mechanism as function of $B_\parallel$ is the in-plane Zeeman energy caused by the number of spins aligned along $B\ \perp$ at the SP of the chimera collapse (Supplementary section S9), we decided to use the skyrmion size as benchmark for the comparison between experiment and theory and not the absolute value of $B_\perp$.

As shown in Fig. 3i–l, we adapted the calculated dI/dV profiles to the measured ones rather precisely by adapting $B_\perp$ using the following method.

The dI/dV contrast of a skyrmion consists of two main contributions. The first one is the NCMR contrast (change of local density of states by spin mixing via the canting of neighboring atomic spins [23, 25, 47, 56]), that dominates in our measurements. The second, one is the tunneling magnetoresistance (TMR) as usually employed for SP-STM (spin conserving tunneling between ferromagnetic sample and antiferromagnetic Cr tip providing a spin-polarized atom at its apex [39]) being smaller in our measurements. We neglect the very small third contribution by tunneling anisotropic magnetoresistance [23, 47]. We start with the atomistic 2D magnetization configuration of $\mathbf{m}_i$ at positions $\mathbf{r}_i$ as obtained via the GNEB calculations. We determine dI/dV probed by the tip at position $\mathbf{r}_\mathrm{T}$ by considering the dI/dV signal of each sample atom at $\mathbf{r}_i$ as decaying exponentially towards the tip leading to [25]

$$\frac{dI}{dV}(V, \mathbf{r}_T) = \sum_i \left(\frac{dI}{dV}\right)_i^{loc}(V) \cdot \exp(-2\kappa|\mathbf{r}_\mathrm{T} - \mathbf{r}_i|)$$

with a single decay constant $\kappa = \sqrt{\frac{2m_e\Phi}{\hbar^2}}$, sample work function Φ, bare electron mass m_e, and Planck's constant $\hbar$. The tip position $\mathbf{r}_\mathrm{T}$ is changed laterally at constant height z_0 above the plane of atomic centers of the surface layer. We adapt z_0 and Φ using experimental $I(z)$ curves recorded with the same tip at the same V as the dI/dV maps. We set $z_0 = 0$ pm via $I(z_0 = 0)/V = 2e^2/h$ using continuation of the $I(z)$ curves. This reveals $\Phi = 4.8$ eV and $z_0 = 600$ pm for Fig. 3a–d (Extended data Fig. 2a–d).

Crucially, $(dI/dV)_i^{loc}$, i.e., the $dI/dV(V)$ contribution of each atom i projected to its position in the surface layer, contains the convolution of non-spin-polarized local density of states $(dI/dV)_0$ and the spin-dependent parts originating from NCMR and TMR as described by the scaling factors γ_NCMR and γ_TMR [25]:

$$\left(\frac{dI}{dV}\right)_i^{loc}(V) = \frac{dI}{dV}_0(V) \cdot (1 + \gamma_\mathrm{NCMR} \cdot \angle_i^{NN} + \gamma_\mathrm{TMR} \cdot \mathbf{m}_i \cdot \mathbf{m}_\mathrm{T}). \quad (5)$$

The magnetization vector $\mathbf{m}_\mathrm{T}$ of the tip atom is scaled to unity length as the $\mathbf{m}_i$. The NCMR component [23] is approximated as depending on $\angle_i^{NN}$, the mean angle of each $\mathbf{m}_i$ to its 6 nearest neighbors $\mathbf{m}_j$ [25]. The TMR depends on the canting between $\mathbf{m}_i$ and $\mathbf{m}_\mathrm{T}$.
In order to reproduce the dI/dV maps of the experiment, we adapt γ_NCMR, γ_TMR, dI/dV_0, and the angles of the tip magnetization θ and ϕ, with $\phi = 0$ chosen parallel to $B_\parallel$: $\mathbf{m}_T = (\cos\phi \cdot \sin\theta, \sin\phi \cdot \sin\theta, \cos\theta)$. We use a cut-off at $3 \cdot z_0$ for the maximum distance of contributing sample atoms ($\mathbf{m}_i$) relative to the tip atom. Primarily, we changed $B_\perp$ in the atomistic spin simulations until the lateral extension of the dI/dV contrast of experiment and simulation matched. Afterwards, we adapted the other parameters. The stronger NCMR contrast was adapted firstly via γ_NCMR and dI/dV_0, the latter read directly from the dI/dV value of the surrounding ferromagnetic area of the skyrmion. The remaining three parameters (γ_TMR, θ, ϕ) were only employed afterwards to optimize profile lines (Extended Data Fig. 2m−p).

Extended Data Figs. 2a−l show the resulting simulated dI/dV images in comparison with the measured ones as well as the GNEB based magnetization maps of the corresponding skyrmions. The best agreement has been achieved using $B_\perp = 3.2\,\mathrm{T}$ and for

Extended Data Fig. 2e:
$\gamma_\mathrm{NCMR} = -0.48$, $\gamma_\mathrm{TMR} = 0.044$, $\theta = 155°$, $\phi = 350°$.

Extended Data Fig. 2f:
$\gamma_\mathrm{NCMR} = -0.48$, $\gamma_\mathrm{TMR} = 0.044$, $\theta = 135°$, $\phi = 350°$.

Extended Data Fig. 2g,h:
$\gamma_\mathrm{NCMR} = -0.66$, $\gamma_\mathrm{TMR} = 0.040$, $\theta = 155°$, $\phi = 350°$.

Small differences in the parameters for different images are attributed to minor tip changes during the sequence of measurements. Note that we mostly had a dominating out-of-plane contribution to the TMR contrast (82% in Extended Data Figs. 2e,g,h) such that adapting ϕ is of negligible influence.

Hence, an increased $B_\perp$ in the atomistic spin simulations is sufficient to adapt the profiles, while $B_\parallel$ could be left as in the experiment. We used the resulting spin configurations of the calculations to determine the radius r of the skyrmion by defining the skyrmion circumference at the spins that are tilted by 10° relative to $B_\perp$. Application of $B_\parallel$ did not change r via this definition, but shifted the out-of-plane spins within the circle by about one atom (Extended Data Fig. 2 i-l). Since the shape of the circumference additionally gets slightly elliptic with $B_\parallel$, we kept the radius and center position of the skyrmion from the determination at $B_\parallel = 0\,\mathrm{T}$. This simplification is irrelevant for our conclusions.

Calculation of minimum energy paths. A minimum energy path (MEP) connecting two stable states on the energy surface is defined in such a way that the energy is minimal with respect to the transverse displacements of the path. Although the MEP is not a dynamical trajectory, it is a path of highest statistical weight and, therefore, gives a convenient representation of a particular mechanism of the transition between the states. The geodesic nudged elastic band (GNEB) method [40] was used to find MEPs for the skyrmion collapse. A path is represented by a discrete chain of states, so-called images, that interpolate between the isolated skyrmion, that is relaxed by spin dynamics simulations and the velocity projection optimization method [40], and the ferromagnetic state. The images are connected by artificial spring forces so as to control the distribution along the path. The strength of the spring force for image k caused by image l depends on the geodesic distance in the configuration space D_geo and on the energy difference D_en between adjacent images via

$$F_\mathrm{spring}^{k,l} = \kappa \sqrt{\left(D_\mathrm{geo}^{k,l}\right)^2 + \kappa_\mathrm{en}\left(D_\mathrm{en}^{k,l}\right)^2}. \qquad (6)$$

Here, the spring constant κ is chosen to be 0.1 meV/rad^2. The measures of distance D_geo and D_en are in units of rad and meV and their relative weight is controlled by the chosen parameter $\kappa_\mathrm{en} = 0.01$ rad^2/meV^2. The extension of the method by taking D_en into account is necessary to obtain a sufficient number of images close to the SP of the chimera transition mechanism. This ensures a better resolution and convergence behavior of the method.

In order to obtain metastable paths, first, an initial path is created by geodesic rotation from the initial to the final state that is additionally disturbed by small random fluctuations to avoid a path that is too symmetric to form an energy gradient. The GNEB relaxation of the geodesic path tends to converge into the radial symmetric annihilation mechanism for small $B_\parallel$ and large $B_\perp$, while it converges more often into the chimera type mechanism vice versa. Starting from these MEP configurations, $B_\parallel$ is successively decreased (increased) for the radial symmetric (chimera) mechanism, yielding relaxed metastable MEPs with varying $B_\parallel$ for both collapse mechanisms. Finally, a climbing image method is used to find the SP of the MEP. Different energetic contributions to the MEP and the SP are shown in Extended Data Figs. 4/5 and are discussed in Supplementary sections S8/S9.

Calculation of skyrmion collapse and creation rates. The rates of thermally activated transitions from the isolated skyrmion state to the ferromagnetic state (and vice versa) are calculated in the framework of harmonic transition state theory, and therefore has the form of an Arrhenius law [34, 41], i.e. Eq. (1). The energy barrier ΔE of a MEP is provided by the energy difference between the SP and the initial state. By representing excitations of a state in harmonic approximation and in the eigenbasis of the corresponding Hessian, the prefactor ν_0 reads:

$$\nu_0 = \eta \frac{\lambda}{V} k_\mathrm{B} T \frac{\prod_i \sqrt{\epsilon_{\mathrm{SK},i}}}{\prod_i{}' \sqrt{\epsilon_{\mathrm{SP},i}}}. \qquad (7)$$

Here, ϵ_i are the eigenvalues of the Hessian and λ is the dynamical factor defining the system's velocity along the

unstable mode. The prime indicates that the negative eigenvalue corresponding to the unstable mode is excluded from the product. For the skyrmion state, two translational modes exhibit a sufficiently constant energy to be treated as Goldstone modes. They enter the prefactor via the volume V per unit cell [52]. In contrast, in-plane translations of magnetic structure at the SP corresponding to both the radial symmetric collapse and the chimera mechanism are not energetically degenerate due to the presence of a defect whose size is comparable with the lattice constant. Thus, the corresponding modes are treated in harmonic approximation. For both collapse mechanisms, there are two equivalent SPs per unit cell as taken into account by a factor $\eta = 2$ in Eq. (7). Unequal numbers of the Goldstone modes at the SP and at the skyrmion state lead to the linear temperature dependence of the prefactor. Additionally, motion of the Bloch point-like defect along the skyrmion's circumference in the chimera collapse shows a potential Goldstone behavior at zero $B_{\parallel}$. However, application of the in-plane magnetic field breaks this symmetry. As a consequence, the corresponding mode is also treated in harmonic approximation in our calculations.

Calculated skyrmion creation rates are shown in Extended Data Fig. 7 and discussed in Supplementary Section S11.

Calculation of the topological charge We calculate the topological charge Q_{topo} on a discrete lattice [57] reading

$$Q_{\text{topo}} = \sum_i A_i, \tag{8}$$

where A_i is the topological charge per triangle formed by three adjacent magnetic moments $\mathbf{m}_j, \mathbf{m}_k, \mathbf{m}_l$ with i running over all triangles of the hexagonal lattice. The charge per triangle is calculated by [57]

$$\cos(2\pi A_i) = \frac{1 + \mathbf{m}_j \cdot \mathbf{m}_k + \mathbf{m}_j \cdot \mathbf{m}_l + \mathbf{m}_k \cdot \mathbf{m}_l}{\sqrt{2\,(1 + \mathbf{m}_j \cdot \mathbf{m}_k)\,(1 + \mathbf{m}_j \cdot \mathbf{m}_l)\,(1 + \mathbf{m}_k \cdot \mathbf{m}_l)}}, \tag{9}$$

with $\operatorname{sgn}(A_i) = \operatorname{sgn}[\mathbf{m}_j \cdot (\mathbf{m}_k \times \mathbf{m}_l)]$.

Calculation of temperature profiles after hot electron injection.

We employed a finite element method as implemented in Solid Works using the temperature dependent heat capacity $c_p(T)$ and heat conductivity $\kappa(T)$ of Pd within a virtually semi-infinite slab ($20 \times 20 \times 15$ nm^3). The starting configuration deposits the energy of a single hot electron (0.61 eV) in a disk of radius 0.25 nm and height of one atomic layer that is surrounded by a temperature of 6 K. We use a grid size of half an atomic distance and time steps of 0.5 fs for the calculations keeping all boundary cells except the ones at the surface at $T = 6$ K. For the sake of simplicity, we employ standard $\kappa(T)$ and $c_p(T)$ including the phonon contribution, albeit equilibration times between hot electrons and the phonon bath are typically longer than a few fs [58, 59]. This simplification keeps the parameters of the calculation as few as possible, in particular, concerning the complex simulation of heat conduction of hot electrons and magnons. However, we keep in mind that the resulting temperature distribution remains a rough estimate, partly justified, since compared with theoretical calculations that assume an equilibrium temperature across the whole area of the calculation distinct from the regarded dynamics around a local hot spot only (more details and an estimate of validity of the model at such short time scales: Supplementary section S7).

[1] Muhlbauer, S. *et al.* Skyrmion lattice in a chiral magnet. *Science* **323**, 915–919 (2009).

[2] Yu, X. Z. *et al.* Real-space observation of a two-dimensional skyrmion crystal. *Nature* **465**, 901–904 (2010).

[3] Fert, A., Reyren, N. & Cros, V. Magnetic skyrmions: advances in physics and potential applications. *Nat. Rev. Mater.* **2**, 17031 (2017).

[4] Fert, A., Cros, V. & Sampaio, J. Skyrmions on the track. *Nat. Nanotechnol.* **8**, 152–156 (2013).

[5] Heinze, S. *et al.* Spontaneous atomic-scale magnetic skyrmion lattice in two dimensions. *Nat. Phys,* **7**, 713–718 (2011).

[6] Jiang, W. *et al.* Blowing magnetic skyrmion bubbles. *Science* **349**, 283–286 (2015).

[7] Woo, S. *et al.* Observation of room-temperature magnetic skyrmions and their current-driven dynamics in ultrathin metallic ferromagnets. *Nat. Mater.* **15**, 501–506 (2016).

[8] Legrand, W. *et al.* Room-temperature current-induced generation and motion of sub-100 nm skyrmions. *Nano Lett.* **17**, 2703–2712 (2017).

[9] Song, K. M. *et al.* Skyrmion-based artificial synapses for neuromorphic computing. *Nat. Electr.* **3**, 148–155 (2020).

[10] Abanov, A. & Pokrovsky, V. L. Skyrmion in a real magnetic film. *Phys. Rev. B* **58**, R8889–R8892 (1998).

[11] Cai, L., Chudnovsky, E. M. & Garanin, D. A. Collapse of skyrmions in two-dimensional ferromagnets and antiferromagnets. *Phys. Rev. B* **86**, 024429 (2012).

[12] Milde, P. *et al.* Unwinding of a skyrmion lattice by magnetic monopoles. *Science* **340**, 1076–1080 (2013).

[13] Je, S.-G. *et al.* Direct demonstration of topological stability of magnetic skyrmions via topology manipulation. *ACS Nano* **14**, 3251–3258 (2020).

[14] Varentsova, A., Potkina, M., von Malottki, S., Heinze, S. & Bessarab, P. Interplay between size and stability of magnetic skyrmions. *Nanosystems: Phys., Chem., Math.* 356–363 (2018).

[15] Wild, J. *et al.* Entropy-limited topological protection of skyrmions. *Sci. Adv.* **3**, e1701704 (2017).

[16] Zázvorka, J. *et al.* Thermal skyrmion diffusion used in a reshuffler device. *Nat. Nanotechnol.* **14**, 658–661 (2019).

[17] Woo, S. *et al.* Deterministic creation and deletion of a sin-

gle magnetic skyrmion observed by direct time-resolved X-ray microscopy. *Nat. Electr.* **1**, 288–296 (2018).

[18] Chen, G., Mascaraque, A., N'Diaye, A. T. & Schmid, A. K. Room temperature skyrmion ground state stabilized through interlayer exchange coupling. *Appl. Phys. Lett.* **106**, 242404 (2015).

[19] Seki, S., Yu, X. Z., Ishiwata, S. & Tokura, Y. Observation of skyrmions in a multiferroic material. *Science* **336**, 198–201 (2012).

[20] Dovzhenko, Y. *et al.* Magnetostatic twists in room-temperature skyrmions explored by nitrogen-vacancy center spin texture reconstruction. *Nat. Commun.* **9**, 2712 (2018).

[21] Grenz, J., Köhler, A., Schwarz, A. & Wiesendanger, R. Probing the nano-skyrmion lattice on Fe/Ir(111) with magnetic exchange force microscopy. *Phys. Rev. Lett.* **119**, 047205 (2017).

[22] Romming, N. *et al.* Writing and deleting single magnetic skyrmions. *Science* **341**, 636–639 (2013).

[23] Hanneken, C. *et al.* Electrical detection of magnetic skyrmions by tunnelling non-collinear magnetoresistance. *Nat. Nanotechnol.* **10**, 1039–1042 (2015).

[24] Hervé, M. *et al.* Stabilizing spin spirals and isolated skyrmions at low magnetic field exploiting vanishing magnetic anisotropy. *Nat. Commun.* **9**, 1015 (2018).

[25] Meyer, S. *et al.* Isolated zero field sub-10 nm skyrmions in ultrathin Co films. *Nat. Commun.* **10**, 3823 (2019).

[26] Büttner, F. *et al.* Dynamics and inertia of skyrmionic spin structures. *Nat. Phys.* **11**, 225–228 (2015).

[27] Woo, S. *et al.* Spin-orbit torque-driven skyrmion dynamics revealed by time-resolved X-ray microscopy. *Nat. Commun.* **8**, 15573 (2017).

[28] Litzius, K. *et al.* Skyrmion hall effect revealed by direct time-resolved X-ray microscopy. *Nat. Phys.* **13**, 170–175 (2016).

[29] Hsu, P.-J. *et al.* Electric-field-driven switching of individual magnetic skyrmions. *Nat. Nanotechnol.* **12**, 123–126 (2016).

[30] Büttner, F. *et al.* Field-free deterministic ultrafast creation of magnetic skyrmions by spin–orbit torques. *Nat. Nanotechnol.* **12**, 1040–1044 (2017).

[31] Hagemeister, J., Romming, N., von Bergmann, K., Vedmedenko, E. Y. & Wiesendanger, R. Stability of single skyrmionic bits. *Nat. Commun.* **6**, 8455 (2015).

[32] Hanneken, C., Kubetzka, A., von Bergmann, K. & Wiesendanger, R. Pinning and movement of individual nanoscale magnetic skyrmions via defects. *New J. Phys.* **18**, 055009 (2016).

[33] von Malottki, S., Bessarab, P. F., Haldar, S., Delin, A. & Heinze, S. Skyrmion lifetime in ultrathin films. *Phys. Rev. B* **99**, 060409 (2019).

[34] Bessarab, P. F. *et al.* Lifetime of racetrack skyrmions. *Sci. Rep.* **8**, 3433 (2018).

[35] von Malottki, S., Dupé, B., Bessarab, P. F., Delin, A. & Heinze, S. Enhanced skyrmion stability due to exchange frustration. *Sci. Rep.* **7**, 12299 (2017).

[36] Paul, S., Haldar, S., von Malottki, S. & Heinze, S. Role of higher-order exchange interactions for skyrmion stability. *arXiv:* **1912.03474** (2019).

[37] Uzdin, V., Potkina, M., Lobanov, I., Bessarab, P. & Jónsson, H. Energy surface and lifetime of magnetic skyrmions. *J. Magn. Magn. Mater.* **459**, 236–240 (2018).

[38] Desplat, L., Kim, J.-V. & Stamps, R. L. Paths to annihilation of first- and second-order (anti)skyrmions via (anti)meron nucleation on the frustrated square lattice. *Phys. Rev. B* **99**, 174409 (2019).

[39] Bode, M. Spin-polarized scanning tunnelling microscopy. *Rep. Prog. Phys.* **66**, 523–582 (2003).

[40] Bessarab, P. F., Uzdin, V. M. & Jónsson, H. Method for finding mechanism and activation energy of magnetic transitions, applied to skyrmion and antivortex annihilation. *Comp. Phys. Comm.* **196**, 335–347 (2015).

[41] Bessarab, P. F., Uzdin, V. M. & Jónsson, H. Harmonic transition-state theory of thermal spin transitions. *Phys. Rev. B* **85**, 184409 (2012).

[42] Rohart, S., Miltat, J. & Thiaville, A. Path to collapse for an isolated Néel skyrmion. *Phys. Rev. B* **93**, 214412 (2016).

[43] Romming, N., Kubetzka, A., Hanneken, C., von Bergmann, K. & Wiesendanger, R. Field-dependent size and shape of single magnetic skyrmions. *Phys. Rev. Lett.* **114**, 177203 (2015).

[44] Fernandes, I. L., Bouaziz, J., Blügel, S. & Lounis, S. Universality of defect-skyrmion interaction profiles. *Nat. Commun.* **9**, 4395 (2018).

[45] Krause, S., Berbil-Bautista, L., Herzog, G., Bode, M. & Wiesendanger, R. Current-induced magnetization switching with a spin-polarized scanning tunneling microscope. *Science* **317**, 1537–1540 (2007).

[46] Bessarab, P. F., Uzdin, V. M. & Jónsson, H. Size and shape dependence of thermal spin transitions in nanoislands. *Phys. Rev. Lett.* **110**, 020604 (2013).

[47] Kubetzka, A., Hanneken, C., Wiesendanger, R. & von Bergmann, K. Impact of the skyrmion spin texture on magnetoresistance. *Phys. Rev. B* **95**, 104433 (2017).

[48] Kubetzka, A., Bode, M., Pietzsch, O. & Wiesendanger, R. Spin-polarized scanning tunneling microscopy with antiferromagnetic probe tips. *Phys. Rev. Lett.* **88**, 057201 (2002).

[49] Mashoff, T., Pratzer, M. & Morgenstern, M. A low-temperature high resolution scanning tunneling microscope with a three-dimensional magnetic vector field operating in ultrahigh vacuum. *Rev. Sci. Instr.* **80**, 053702 (2009).

[50] Holl, C. *et al.* Probing the pinning strength of magnetic vortex cores with sub-nanometer resolution. *Nat. Commun.* **11**, 2833 (2020).

[51] Dupé, B., Hoffmann, M., Paillard, C. & Heinze, S. Tailoring magnetic skyrmions in ultra-thin transition metal films. *Nat. Commun.* **5**, 4030 (2014).

[52] Haldar, S., von Malottki, S., Meyer, S., Bessarab, P. F. & Heinze, S. First-principles prediction of sub-10-nm skyrmions in Pd/Fe bilayers on Rh(111). *Phys. Rev. B* **98**, 060413 (2018).

[53] Böttcher, M., Heinze, S., Egorov, S., Sinova, J. & Dupé, B. B–T phase diagram of Pd/Fe/Ir (111) computed with parallel tempering Monte Carlo. *New J. Phys.* **20**, 103014 (2018).

[54] Lindner, P. *et al.* Temperature and magnetic field dependent behavior of atomic-scale skyrmions in Pd/Fe/Ir(111) nanoislands. *Phys. Rev. B* **101**, 214445 (2020).

[55] Heil, B., Rosch, A. & Masell, J. Universality of annihilation barriers of large magnetic skyrmions in chiral and frustrated magnets. *Phys. Rev. B* **100**, 134424 (2019).

[56] Crum, D. M. *et al.* Perpendicular reading of single confined magnetic skyrmions. *Nat. Commun.* **6**, 8541 (2015).

[57] Müller, G. P. *et al.* Spirit: Multifunctional framework

for atomistic spin simulations. *Phys. Rev. B* **99**, 224414 (2019).
[58] Elsayed-Ali, H. E., Norris, T. B., Pessot, M. A. & Mourou, G. A. Time-resolved observation of electron-phonon relaxation in copper. *Phys. Rev. Lett.* **58**, 1212–1215 (1987).
[59] Groeneveld, R. H. M., Sprik, R. & Lagendijk, A. Femtosecond spectroscopy of electron-electron and electron-phonon energy relaxation in Ag and Au. *Phys. Rev. B* **51**, 11433–11445 (1995).

DATA AVAILABILITY

Source data are available for this paper. All other data that support the plots within this paper and other findings of this study are available from the corresponding author upon reasonable request.

CODE AVAILABILITY.

All codes used to evaluate the data are available from the corresponding author upon request.

ACKNOWLEDGMENTS

We gratefully acknowledge helpful discussions with S. Lounis, S. Blügel, G. Volovskiy, A. Schlenhoff, M. Liebmann, M. A. Goerzen, T. Sigurjónsdóttir and financial support by the German Science Foundation (DFG) via PR 1098/1-1, the Russian Science Foundation (Grant No. 19-72-10138), the Icelandic Research Fund (Grant No. 184949-052), and the Alexander von Humboldt Foundation.

AUTHOR CONTRIBUTIONS

F. M. and B. P. conducted the experiments supervised by C. H., M. P. and M. M.. S. v. M. performed all atomistic spin simulations supervised by P. F. B. and S. H.. F. M. and M. M. provided the original idea of the experiment with P. F. B. and S. v. M. coming up with the idea of a more detailed comparison with DFT based calculations. In particular, S. v. M., P. F. B., and S. H. introduced the chimera mode as an explanation of the experimental data. F. M. with the help of C. H. evaluated all experimental data, performed comparisons to calculated data and conducted the calculations of heat distribution of a hot electron. M. M. wrote the first version of the manuscript with image supply by F. M. and S. v. M.. All authors contributed to multiple discussions and the final version of the manuscript.

COMPETING INTERESTS

The authors declare no competing interests.

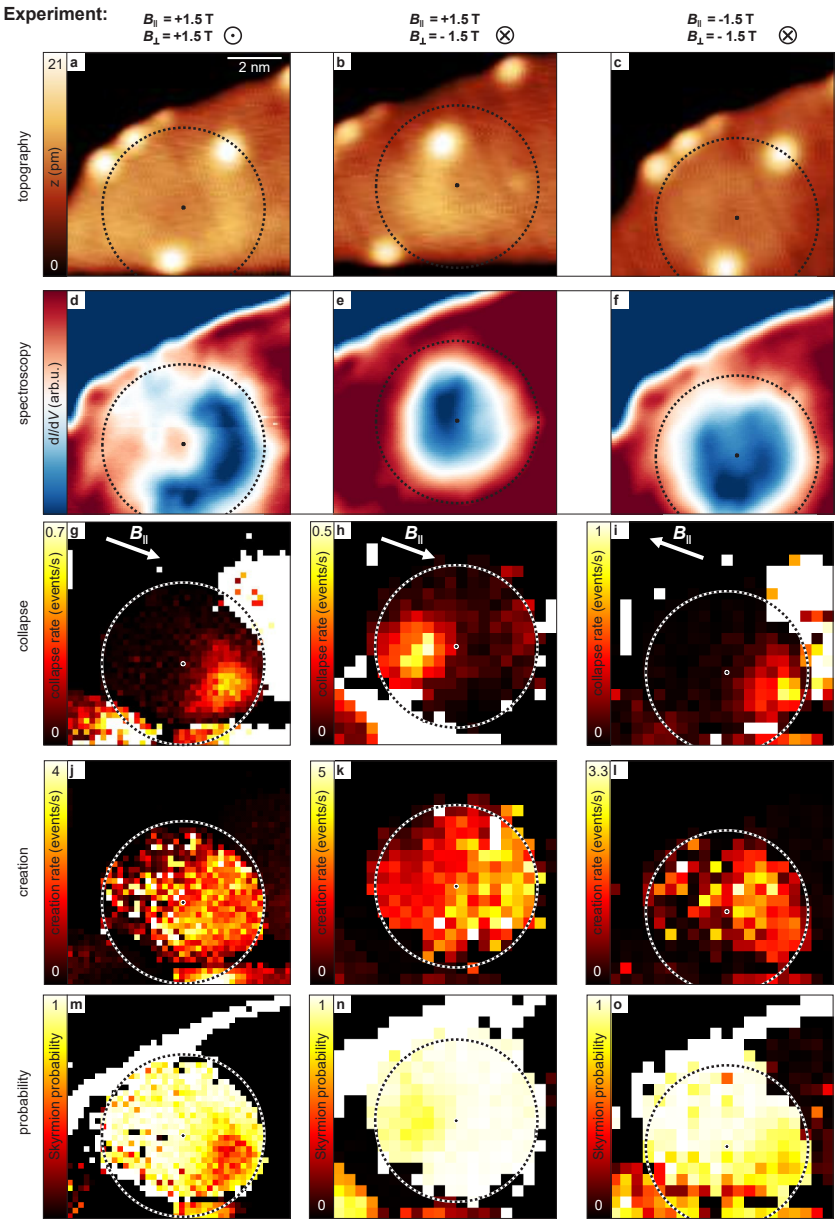

Extended Data Fig. 1. **Switching maps for skyrmion B marked in Fig. 6a).** Images in each column are recorded at the same $B_\parallel$ and $B_\perp$ indicated on top. **a**−**c**, STM topography, $V = 610\,\mathrm{mV}$, $I = 2\,\mathrm{nA}$. Circles mark the skyrmion area with black dot as center. Defects (bright dots) at the skyrmion rim are visible. The skyrmion slightly shifts between images in contrast to skyrmion A (Supplementary Section S1). **d**−**f**, Simultaneously recorded dI/dV maps. **g**−**i**, Maps of skyrmion collapse rates as deduced from time traces recorded at each pixel (Extended Data Fig. 3), $\Delta t = 150\,\mathrm{s}$, $V = 610\,\mathrm{mV}$, $I = 200\,\mathrm{nA}$. The direction of $B_\parallel$ is marked. As in Fig. 3, the hot spot at the rim switches position along $B_\parallel$ by sign change of $B_\perp$ or $B_\parallel$ and is always located close to the darkest spot within the corresponding dI/dV images. **j**−**l**, Maps of creation rates obtained from the same time traces, being rather homogeneous in the skyrmion area. **m**−**o**, Maps of skyrmion probability P_{SK} obtained from the same time traces. The probability close to one shows that the skyrmion state is more stable than the ferromagnetic state. Circles are at identical positions in each column.

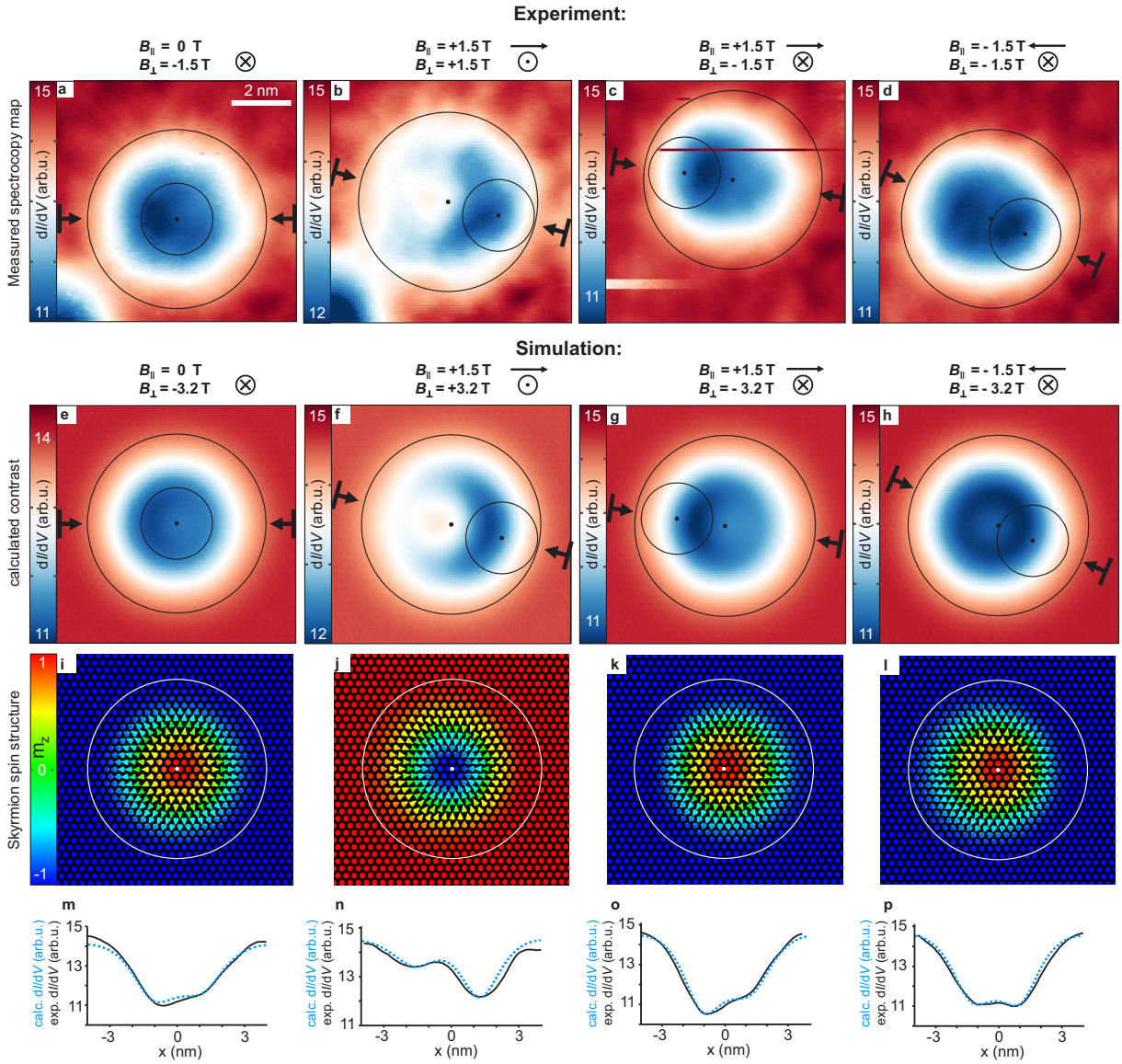

Extended Data Fig. 2. **Adapting dI/dV contrast from atomistic spin simulations to experimental dI/dV maps. a-d**, Measured dI/dV maps of skyrmion A (Fig. 6a) at the **B** fields marked on top (same as Fig. 3a–d). Large (small) circles enclose the skyrmion area (hot spot of collapse rate) with dot as circle center. Arrows mark directions of profile lines in (m)–(p). **e-h**, Calculated dI/dV maps consisting of overlapping contributions of NCMR and tunneling magnetoresistance using the spin configurations of (i)–(l) (methods). Circles and arrows are identical to the images on top. **i-l**, Atomic magnetization vectors $\mathbf{m}_i$ (arrows) with color marking m_i^z as calculated by the atomistic spin model. Circles are identical to the larger circles of the upper images in the same column. (e)–(l) $B_\perp$, $B_\parallel$ as marked above (e)–(h). **m-p**, Profile lines through measured (black) and simulated (dotted blue) dI/dV images at the positions marked by arrows in (a)–(h) (same curves are shown in Fig. 3i–l).

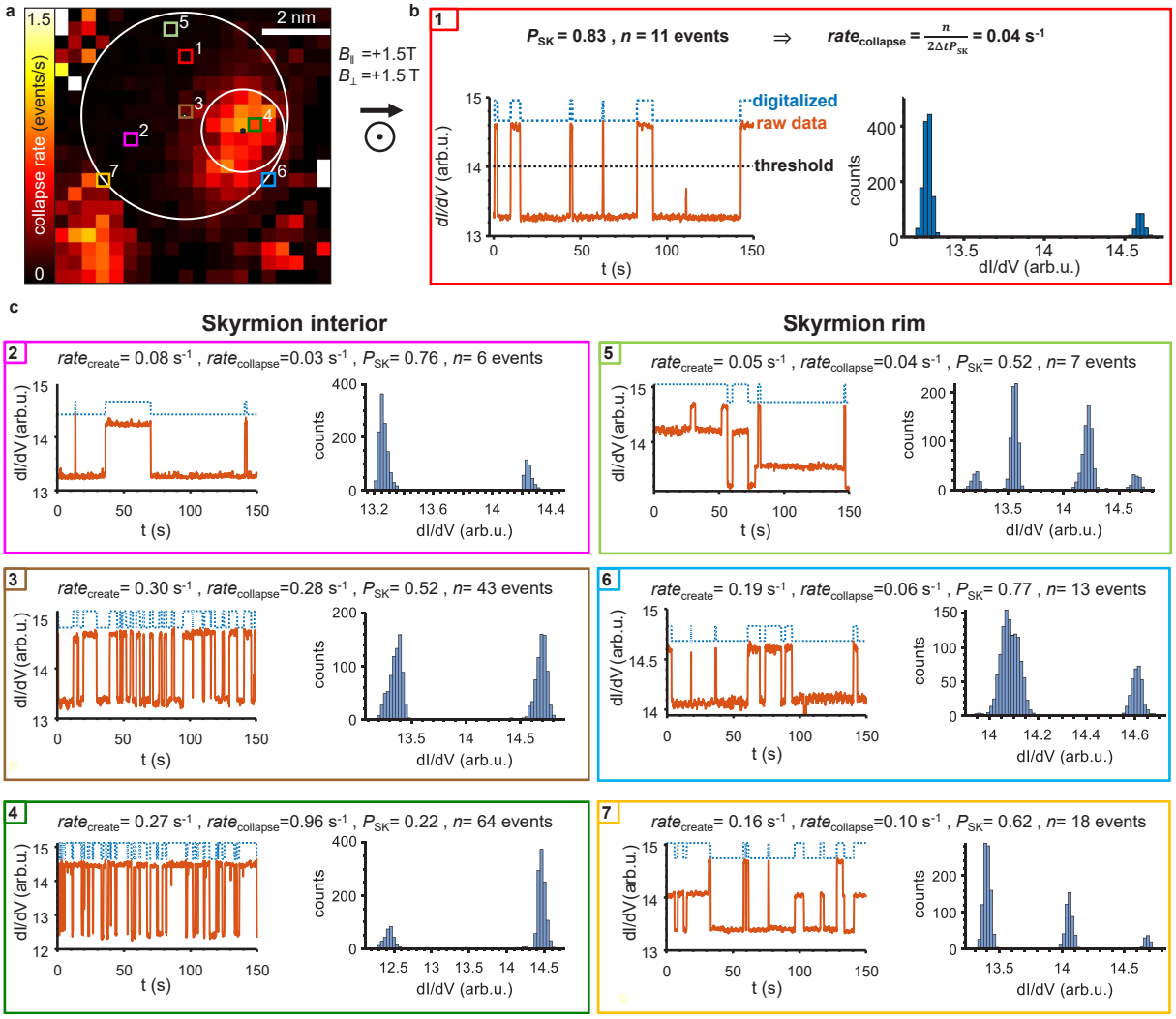

Extended Data Fig. 3. **Telegraph noise in switching maps. a**, Map of skyrmion collapse rate, $B_\parallel = 1.5\,\mathrm{T}$, $B_\perp = 1.5\,\mathrm{T}$, $V = 610\,\mathrm{mV}$, $I = 60\,\mathrm{nA}$, $\Delta t = 150\,\mathrm{s}$ (same as Fig. 3f). Large (small) circle marks skyrmion area (hot spot of collapse rate). Colored rectangles with numbers mark positions, where time traces and histograms are displayed in (b), (c). **b**, Left: time trace (orange curve) on position marked as 1 in (a). The deduced digital values (blue, dashed curve) using a threshold (black, dashed line) are shown with upper (lower) value marking the ferromagnetic (skyrmion) state. The skyrmion probability P_{SK} and the number of switching events n are marked on top. These numbers are used to calculate the collapse rate $rate_{\mathrm{collapse}}$ by the given formula for a time interval Δt of recording. Right: histograms of measured dI/dV values during the time trace. **c**, Time traces as exemplarily shown in (b) (left) and histograms of measured dI/dV values during the time trace (right) for the positions marked in (a) by the same number and frame color. Deduced rates for collapse and creation, skyrmion probability P_{SK} and number of switching events n are marked on top in each frame. Frames are ordered for pixels within the skyrmion interior (left) and at the rim of the skyrmion (right). While the histograms from the interior are always bimodal, additonal peaks partly appear at the rim. They are likely caused by switching of neighboring skyrmions. (More time traces and detailed discussion: Supplementary Fig. S3)

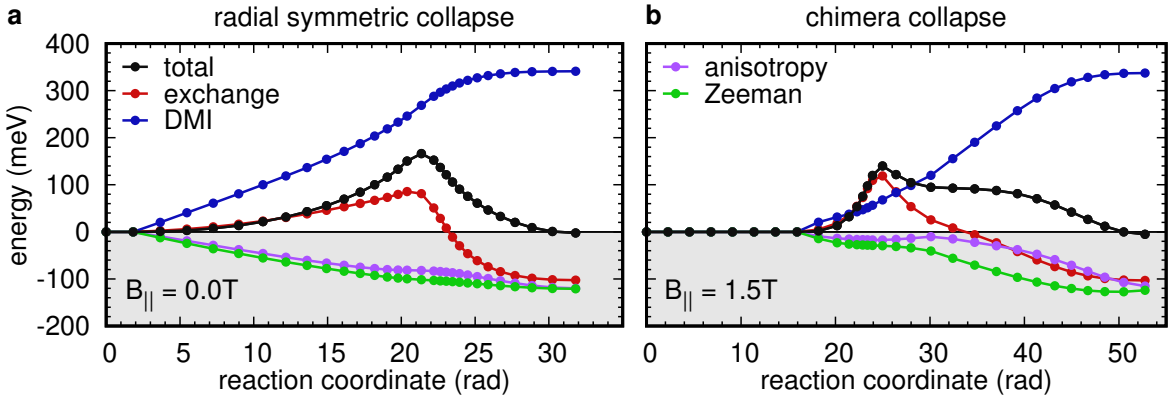

Extended Data Fig. 4. **Calculated minimum energy paths: different energetic contributions. a**, The energy contributions along the minimum energy path given relative to the initial relaxed skyrmion state for the radial symmetric collapse of an isolated skyrmion, $B_\perp = 3.2\,\mathrm{T}$, $B_\parallel = 0.0\,\mathrm{T}$. **b**, Same as (a) for the chimera collapse, $B_\perp = 3.2\,\mathrm{T}$, $B_\parallel = 1.5\,\mathrm{T}$. The legend applies to both images. Black: total energy along the deduced minimum energy path (methods), red: contribution of exchange energy, blue: contribution of Dzyaloshinskii-Moriya interaction (DMI), pink: contribution of magnetocrystalline anisotropy energy, green: contribution of Zeeman energy caused by the applied **B**. The saddle point (SP, maximum of black curve) is dominated by exchange energy in both cases. For (a), the DMI contribution raises from the start, while the anisotropy and exchange energy shrink simultaneously. For (b), the DMI contribution starts rising only shortly prior to the SP, hence contributing much less energy penalty to the SP, while Zeeman and anisotropy contributions barely lower the SP energy and shrink only after the SP has been overcome (detailed analysis in Supplementary Sections S8/S9).

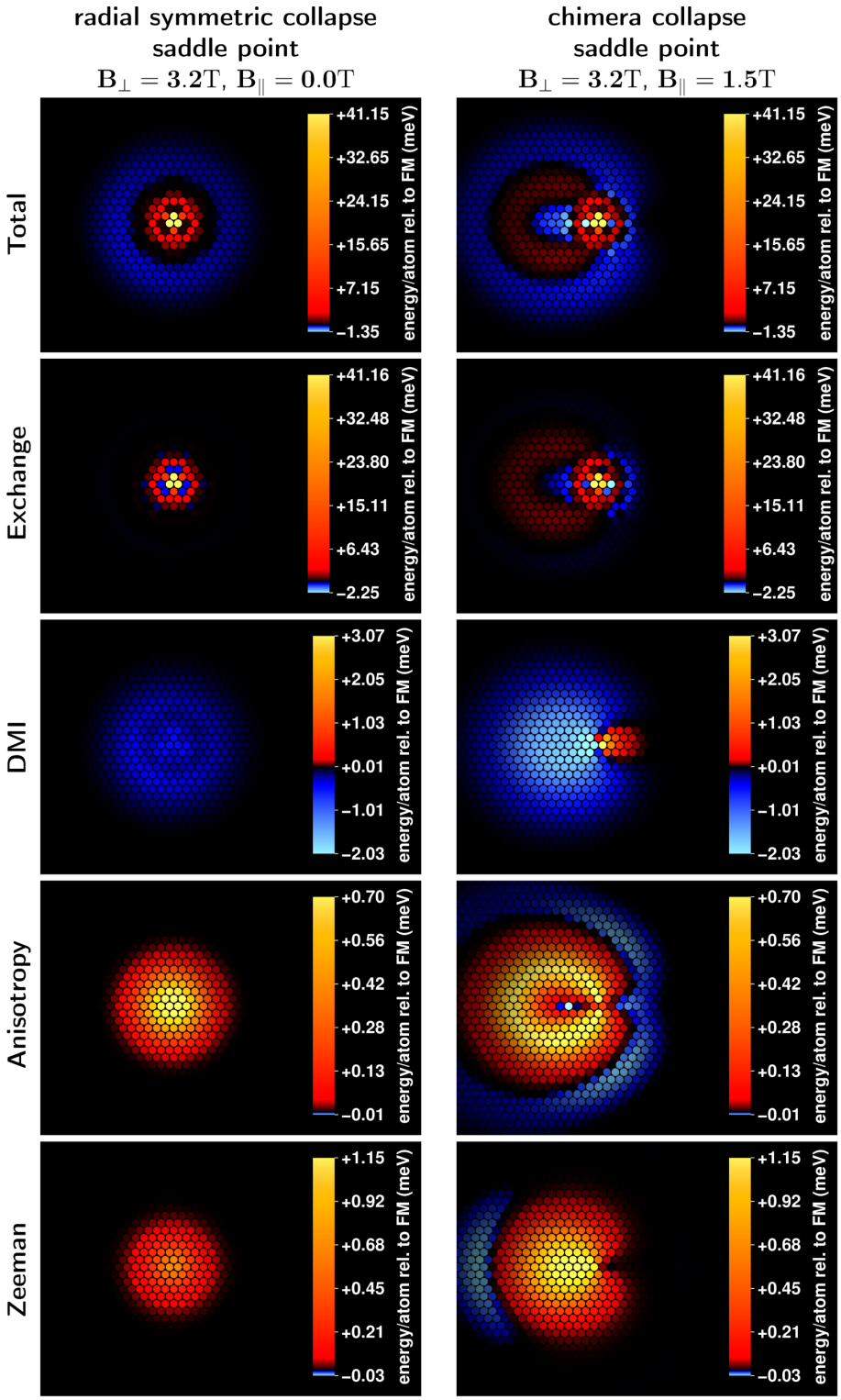

Extended Data Fig. 5. **Energy density maps of different contributions at the saddle points.** Energy densities at the saddle point relative to the relaxed ferromagnetic state (FM) for radial symmetric (left column) and chimera (right column) collapse of an isolated skyrmion at **B** as marked on top. The hot spot is dominated by exchange energy in both cases with minor contributions of Dzyaloshinskii-Moriya interaction (DMI) for the chimera collapse. The total energy lowering by DMI with respect to FM is, however, more extensive for the chimera collapse due to the larger area of adequately winding spins (detailed analysis in Supplementary Sections S8/S9).

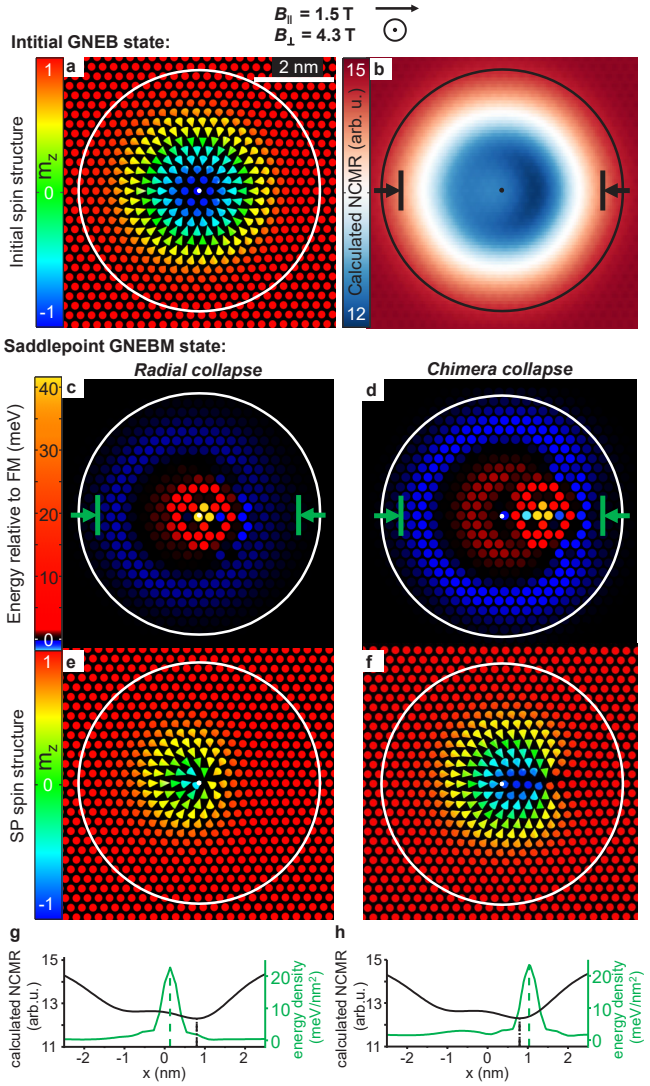

Extended Data Fig. 6. **Comparison of hot spots at saddle point for the same B.** **a**, Magnetization directions of the atoms (arrows) of the skyrmion, relaxed by spin dynamics and the velocity projection optimization method (methods), and colored according to the m_z contribution. The white circle marks the skyrmion radius deduced from calculated dI/dV image (b) (methods). **b**, Simulated dI/dV map of the relaxed skyrmion using the NCMR contrast only [23] (methods). Arrows mark directions and interpolation widths of profile lines in (g,h). **c,d**, Energy density map for the radial symmetric (c) and chimera collapse (d) at the saddle point as calculated by GNEB. The energy is relative to the relaxed ferromagnetic state (FM). **e,f**, Magnetization structure at the saddle point (SP) for radial symmetric (e) and chimera (f) collapse. **g,h**, Profile lines along arrows in (c), (d) for (g), (h), respectively, (green) and along arrows in (b) (black). Dashed lines mark maxima (minima) of the green (black) curves. The maximum of the energy density in (h) is slightly shifted away from the center with respect to the simulated NCMR contrast minimum. While the maximum energy density of the radial collapse remains close to the skyrmion center, it is offset by 1 nm for the chimera collapse (detailed discussion in Supplementary Section S10).

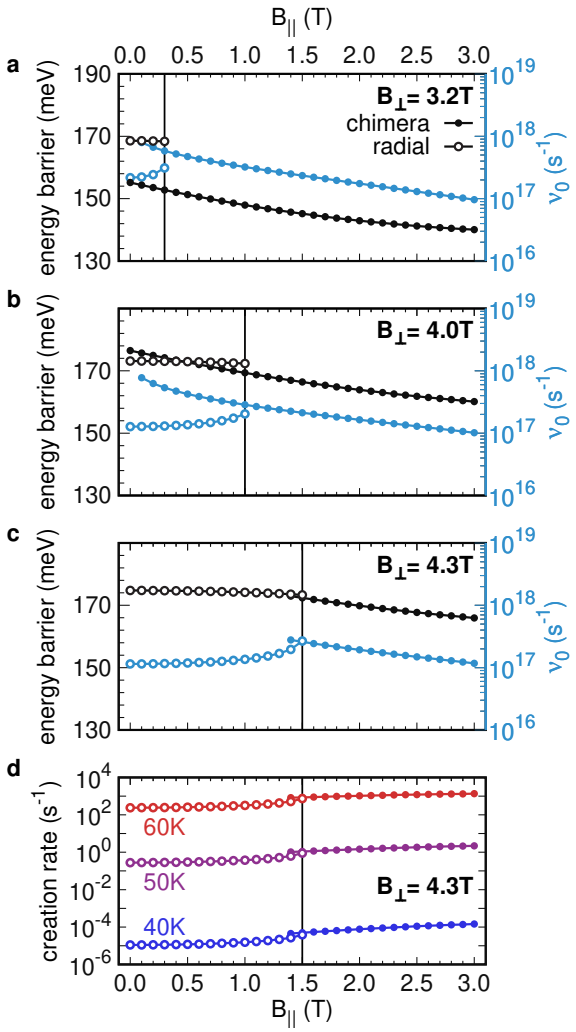

Extended Data Fig. 7. **Calculated energy barriers and prefactors for skyrmion creation. a-c**, Energy barriers (black) and prefactors (blue) for the radial symmetric (open symbols) and chimera type creation (full symbols) of an isolated skyrmion at varying $B_\parallel$ according to atomistic spin simulations via GNEB and transition state theory based on parameters from DFT (methods). (a) $B_\perp = 3.2\,\mathrm{T}$, (b) $B_\perp = 4.0\,\mathrm{T}$, (c) $B_\perp = 4.3\,\mathrm{T}$. **d**, Thermal creation rates at $B_\perp = 4.3\,\mathrm{T}$ resulting from (c) using eq. (1) for three different temperatures with filled (open) circles employing the chimera (radial symmetric) creation process. Trends are similar as for the collapse mechanisms (Fig. 5), but the creation rates (d) depend much less on $B_\parallel$ than the collapse rates (detailed discussion in Supplementary Section S11).

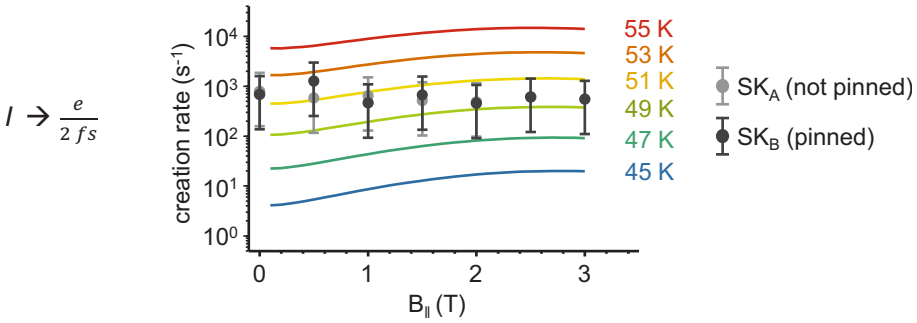

Extended Data Fig. 8. **Comparison of calculated and experimental skyrmion creation rates.** Thermally induced skyrmion creation rates at different T deduced with the help of eq. (1) using the theoretical parameters from atomistic spin simulations of Extended data Fig. 7a (colored lines, $B_\perp = 3.2\,\mathrm{T}$) and experimental skyrmion creation probabilities per single electron (Fig. 6g) extrapolated to creation rates for an assumed $I = e/2\,\mathrm{fs} = 75\,\mu\mathrm{A}$ (symbols, $B_\perp = 1.5\,\mathrm{T}$). This large I would establish a quasi-constant temperature of 45 K within the hot spot area of increased energy density at the SP according to our finite element simulation as displayed in Fig. 6h (detailed discussion in Supplementary Section S11). Experimental data of two skyrmions are displayed exhibiting barely any difference. Error bars result from the uncertainty of the adaption of I to a continuous T.